東京大学学術機関リポジトリ

http://repository.dl.itc.u-tokyo.ac.jp/

Title of Thesis（論文題目）

Study on cargo sorting zones in the *trans*-Golgi network visualized by super-resolution confocal live imaging microscopy
（超解像ライブイメージング顕微鏡 SCLIM を用いた積荷タンパク質の仕分けを司るトランスゴルジ網選別ゾーンの可視化研究）

Name（氏 名）　　Yutaro Shimizu（清水　優太朗）

Additional information（追加情報）：

The major part of this thesis has been published in Nature Communications as an article entitled “Cargo sorting zones in the *trans*-Golgi network visualized by super-resolution confocal live imaging microscopy in plants” by Yutaro Shimizu, Junpei Takagi, Emi Ito, Yoko Ito, Kazuo Ebine, Yamato Komatsu, Yumi Goto, Mayuko Sato, Kiminori Toyooka, Takashi Ueda, Kazuo Kurokawa, Tomohiro Uemura, and Akihiko Nakano (2021,volume 12, article id.1901, https://doi.org/10.1038/s41467-021-22267-0)

この論文の一部は以下のように出版されています。
Yutaro Shimizu, Junpei Takagi, Emi Ito, Yoko Ito, Kazuo Ebine, Yamato Komatsu, Yumi Goto, Mayuko Sato, Kiminori Toyooka, Takashi Ueda, Kazuo Kurokawa, Tomohiro Uemura, and Akihiko Nakano. Cargo sorting zones in the *trans*-Golgi network visualized by super-resolution confocal live imaging microscopy in plants. Nature Communications. 2021, 12, 1901.
DOI:　https://doi.org/10.1038/s41467-021-22267-0
URL:　https://www.nature.com/articles/s41467-021-22267-0

Doctoral Dissertation

博士論文

Study on cargo sorting zones in the *trans*-Golgi network visualized by super-resolution confocal live imaging microscopy

（超解像ライブイメージング顕微鏡 SCLIM を用いた 積荷タンパク質の仕分けを司るトランスゴルジ網選別ゾーンの可視化研究）

A Dissertation Submitted for the Degree of Doctor of Philosophy

December 2020

令和 2 年 12 月博士（理学）申請

Department of Biological Sciences, Graduate School of Science,

The University of Tokyo

東京大学大学院理学系研究科

生物科学専攻

Yutaro Shimizu

清水　優太朗

Abstract

In all eukaryotes, transport of proteins to appropriate cellular compartments by membrane trafficking is essential for proper functions of organelles and cells. The *trans*-Golgi network (TGN) has been known as a key platform to sort and transport proteins to their final destinations in post-Golgi membrane trafficking. However, how the TGN sorts proteins with different destinies still remains elusive. To gain an insight into the mechanisms underlying sorting of secretory and vacuolar cargo proteins at the TGN, I examined 3D localization and 4D dynamics of the TGN-localized proteins of *Arabidopsis thaliana* that are involved in cargo protein transport from the TGN, by using the multicolor high-speed and high-resolution spinning-disk confocal microscopy. Here, I demonstrate that TGN-localized proteins exhibit spatially and temporally distinct distribution. TGN-markers such as the a1 subunit of V-ATPase and Q-SNAREs segregate on the same TGN. VAMP721 (R-SNARE), AP (adaptor protein complex)-1, and clathrin compose an exclusive subregion involved in secretory trafficking, whereas VAMP727 (R-SNARE) and AP-4 compose another subregion involved in vacuolar trafficking on the same TGN. Based on these findings, I propose that the single TGN has at least two subregions, or “zones”, responsible for distinct cargo sorting: the secretory-trafficking zone and the vacuolar-trafficking zone.

Table of Contents

Acknowledgements

First of all, I would like to express my sincerest appreciation to Professor Ichiro Terashima for giving me the opportunity to complete my thesis and for his generous guidance, insightful suggestions and encouragement. I would also like to express my deepest appreciation to Associate Professor Tomohiro Uemura (Ochanomizu University) and Deputy Director Akihiko Nakano (RIKEN RAP) for giving me the opportunity to carry out my research in their laboratories and for supervision and encouragement throughout this study. I wish to thank Professor Sotaro Uemura, Professor Tetsuya Higashiyama, Associate Professor Manabu Yoshida, and Professor Ken Sato for being a part of my thesis examination committee. I thank Professor Karin Schumacher (Heidelberg University, Germany), Lecturer Tomoo Shimada (Kyoto University), Professor Ikuko Hara-Nishimura (Konan University), and Professor Taku Demura (Nara Institute of Science and Technology) for kindly sharing materials. I would like to show my deepest gratitude to Ms. Yumi Goto (RIKEN CSRS), Dr. Mayuko Sato (RIKEN CSRS), and Dr. Kiminori Toyooka (RIKEN CSRS) for performing the electron microscopic analysis. I show my appreciation to Assistant Professor Junpei Takagi (Hokkaido University), Dr. Emi Ito (Ochanomizu University), Dr. Yoko Ito (The University of Bordeaux, France), Assistant Professor Kazuo Ebine (National Institute for Basic Biology), Mr. Yamato Komatsu, Professor Takashi Ueda (National Institute for Basic Biology), and Dr. Kazuo Kurokawa (RIKEN RAP) for technical supports, insightful discussions, and sincere encouragement. I thank all the members of Live Cell Super-Resolution Imaging Reseach Team (RIKEN RAP) and Laboratory of Plant Ecology (The University of Tokyo) for generous and wide-ranging support throughout the years. Finally, I thank my family for their endless love and support along the way.

Abbreviations

AP	adaptor protein
CCV	clathrin-coated vesicle
CHC	clathrin heavy chain
CLC	clathrin light chain
ER	endoplasmic reticulum
GFP	green fluorescent protein
iRFP	infrared fluorescent protein
MVE	multivesicular endosome
PM	plasma membrane
RFP	red fluorescent protein
SCLIM	super-resolution confocal live imaging microscopy
SNARE	Soluble *N*-ethylmaleimide-sensitive factor attachment protein receptors
TGN	*trans*-Golgi network
VAMP	vesicle-associated membrane protein

Chapter 1: Introduction

Eukaryotic cells have various single-membrane-bounded compartments, called organelles, such as the endoplasmic reticulum (ER), the Golgi apparatus, the *trans*-Golgi network (TGN), endosomes, and vacuoles in plant and yeast cells and lysosomes in animal cells. Each of them possesses specific proteins for a distinct function, contributing to the proper maintenance of the cell. Membrane traffic is an important system to transport and localize cargo proteins to the proper compartment. It uses membrane carriers, such as vesicles and tubules, to transport proteins between single-membrane-bounded organelles and the plasma membrane (PM) (Derby & Gleeson, 2007; Saito & Ueda, 2009). It is an evolutionarily conserved system among eukaryotes and consists of 4 fundamental processes; 1) sorting cargo proteins and forming transport carriers on donor organelle membranes, 2) transporting them from the donor to the target organelle membrane, and 3) tethering and 4) fusing them with the target organelle membrane (Fujimoto & Ueda, 2012).

The ER is the entry point for cargo proteins in the membrane traffic, whereas PM and vacuoles are regarded as the final destinations. ER-synthesized cargo proteins destined for the PM/extracellular space or vacuoles are sorted away from ER-resident proteins and enter the Golgi apparatus. The Golgi apparatus usually consists of several flattened membrane-enclosed sacs (called cisternae), which are stacked like pancakes, and plays an important role in post-translational modifications such as glycosylation of cargo proteins. It is divided into three regions—*cis*, medial, and *trans*—each responsible for distinct enzymatic reactions (Glick & Nakano, 2009). The *cis*-most membranous compartment receives newly synthesized cargo proteins from the ER (Glick & Nakano, 2009; Y. Ito & Boutté, 2020; Mellman & Warren, 2000). The cargo proteins are sequentially processed and matured, while they pass through the Golgi apparatus from *cis*- to *trans*-cisternae

(Day et al., 2013; Mellman & Warren, 2000). They then reach the TGN, a membranous compartment adjacent to the *trans*-most Golgi cisterna.

The recognition of the importance of this membranous compartment adjacent to *trans*-most cisterna of the Golgi was first seen in the pioneering work by Novikoff which used electron microscopy (A. B. Novikoff, 1964). He first proposed that lysosomes are formed in this compartment since cytochemical staining showed the presence of acid phosphatase activity, which is the major marker of lysosomes. He claimed that it was a specialized region of smooth ER and termed it GERL (acronym for the Golgi-associated structure that is a part of the ER and forms Lysosomes) (A. B. Novikoff, 1964, 1976; P. M. Novikoff et al., 1971). Novikoff also suggested that lysosomal enzymes synthesized in the ER bypassed the Golgi apparatus and were directly transported to lysosomes via the GERL. In addition, he raised the same hypothesis for secretory proteins delivered to the PM when he observed that immature secretory granules seemed to be budding from the GERL (A. B. Novikoff et al., 1977). However, the accumulating evidence from later studies argued against the continuity of this compartment with the ER (Goldfischer, 1982; Hand, 1980; Rambourg et al., 1979; Roth, 1985). Then, in 1986, Griffiths and Simons proposed the new term "*trans*-Golgi network (TGN)" to describe this compartment, which is widely accepted now (Griffiths & Simons, 1986). The TGN is now considered to be responsible for sorting of cargo proteins with different destinies after they pass through the Golgi apparatus (Y. Ito & Boutté, 2020; Uemura, 2016). As judged by electron microscopy, the TGN produces multiple-type vesicles such as secretory vesicles and clathrin-coated vesicles (CCVs), in contrast to the ER and the Golgi apparatus, where only coat protein complex I (COPI)- and COPII-coated vesicles are produced respectively (Day et al., 2013). In addition, the presence of multiple coat adaptors such as an adaptor protein

complex 1 (AP-1) and AP-4 on the TGN, which form cargo-bearing vesicles, possibly reflects its function as the sorting hub (Dacks & Robinson, 2017; Singh & Jürgens, 2018).

Although most eukaryotes possess the stacked Golgi apparatus (often called simply Golgi) with the TGN, spatial organizations and structures of these organelles are different among species. For example, mammalian Golgi and TGN form a huge complicated structure, called the Golgi ribbon. It is composed of many typical Golgi and TGN stacks (called ministacks) being laterally interconnected with each other (Klumperman, 2011). On the other hand, plant cells under normal conditions organize their Golgi and TGN stacks into structurally simple formations, which can be observed as discrete ministacks scattering in the cytoplasm (Kang et al., 2011; Staehelin & Kang, 2008). Nevertheless, the molecular machinery seems to be similar in these species, albeit with some exceptions (Saito & Ueda, 2009). The development of light microscopic techniques has enabled researchers to observe not only the precise subcellular localization but also dynamics of each ministack in a plant cell (Y. Ito et al., 2018; Uemura et al., 2014). Thus, the plant system is very advantageous for dissecting the localization and the dynamics of Golgi- and TGN-resident proteins by microscopy.

Each process comprising the membrane traffic is strictly regulated by evolutionarily conserved protein families. Soluble *N*-ethylmaleimide-sensitive factor attachment protein receptors (SNAREs) are one such evolutionary conserved protein family, which mediate specific membrane fusion events in membrane trafficking. SNAREs can be divided into two groups, Q-SNAREs and R-SNAREs (Lipka et al., 2007; Saito & Ueda, 2009). Three Q-SNAREs (Qa-, Qb-, and Qc-SNAREs) and one R-SNARE localize on target membrane and transport vesicle membrane, respectively, and form a *trans*-SNARE complex composed of cognate partners on the target compartment (Lipka et al.,

2007; Saito & Ueda, 2009). Specific localization and proper pairing of Q-SNAREs and R-SNARE ensure accurate delivery of transport carriers to their correct destinations (Koike & Jahn, 2019; Lipka et al., 2007; Saito & Ueda, 2009). In *Arabidopsis thaliana,* SYNTAXIN OF PLANTS 41/42/43 (SYP41/42/43) and SYP61 are TGN-localized Qa-SNARE and Qc-SNARE, respectively. (Bassham et al., 2000; Sanderfoot et al., 2001). As R-SNARE, *A. thaliana* harbors 9 vesicle-associated membrane protein7 (VAMP7) members (AtVAMP711–713, 721, 722, 724–727) that function in post-Golgi membrane trafficking (Saito & Ueda, 2009; Uemura et al., 2004). They display different subcellular localization patterns, even though they share high sequence similarity (Saito & Ueda, 2009; Uemura et al., 2004). For example, VAMP721 mainly localizes to the TGN and the PM, mediating secretory trafficking (El Kasmi et al., 2013; Kwon et al., 2008; Uemura et al., 2019; Zhang et al., 2011), whereas VAMP727 mostly localizes to multivesicular endosomes (the prevacuolar compartment) and the vacuolar membrane, mediating vacuolar trafficking (Ebine et al., 2008). In addition, some population of VAMP727 also localizes to the TGN, suggesting that VAMP727 mediates the trafficking from the TGN to the vacuole via multivesicular endosomes (Uemura et al., 2019).

Adaptor protein (AP) complexes are another key protein family of post-Golgi membrane trafficking. They recognize specific amino-acid motifs of cargo proteins and pack them into nascent transport vesicles (Boehm & Bonifacino, 2001; Hirst et al., 2011; D. G. Robinson & Pimpl, 2014; M. S. Robinson & Bonifacino, 2001). AP complexes are evolutionary conserved hetero-tetramer complexes, consisting of two large subunits (β_{1-5} and $\alpha/\gamma/\delta/\varepsilon/\zeta$), a medium subunit ($\mu_{1-5}$), and a small subunit ($\sigma_{1-5}$) (Boehm & Bonifacino, 2001; Hirst et al., 2011; D. G. Robinson & Pimpl, 2014; M. S. Robinson & Bonifacino, 2001). Among 5 types of AP complexes (AP-1–AP-5) at least AP-1 and

AP-4 function in the TGN in *A. thaliana* (Boehm & Bonifacino, 2001; Hirst et al., 2011; Park et al., 2013; D. G. Robinson & Pimpl, 2014; M. S. Robinson & Bonifacino, 2001; Shimada et al., 2018; Teh et al., 2013; J.-G. Wang et al., 2013, 2016, 2017; X. Wang et al., 2014). AP-1 appears to be involved in multiple trafficking pathways from the TGN to the PM and the vacuole (Park et al., 2013; Shimada et al., 2018; Teh et al., 2013; J.-G. Wang et al., 2013, 2016, 2017; X. Wang et al., 2014), whereas AP-4 is involved in trafficking from the TGN to the vacuole (Fuji et al., 2016; Müdsam et al., 2018).

In spite of the knowledge about these key components involved in the trafficking at the TGN, little is known about how the TGN provides venues for sorting of secretory and vacuolar cargos simultaneously. In order to address this question, I have visualized plant TGN-localized proteins—SNAREs, AP complexes, and clathrin—and examined their detailed localization and dynamics at high spatiotemporal resolution. The super-resolution confocal live imaging microscopy (SCLIM), which Nakano and his colleagues developed (Kurokawa et al., 2013, 2019; Nakano, 2013), allows simultaneous multicolor high-speed and high-resolution observations. By the SCLIM observation, I have found that VAMP721/AP-1/clathrin and VAMP727/AP-4 are located on different subregions of a single TGN. I propose to call the subregions composed of VAMP721/AP-1/clathrin and VAMP727/AP-4 “secretory-trafficking zone” and “vacuolar-trafficking zone”, respectively. Furthermore, detailed 4D observations suggest that portions of the secretory-trafficking zone are released from the TGN in the form of clusters of vesicles/buds, containing SYP61, AP-1, clathrin, and VAMP721. These results indicate that the TGN has functional zones specialized for distinct trafficking pathways.

Chapter 2: Materials and Methods

Plant materials and growth conditions. Surface-sterilized seeds were sown on the Murashige and Skoog (MS) medium (1xMS salt, 2% sucrose, 1x Gamborg's vitamin mix and 0.3% phytagel), vernalized at 4°C for two days, and then grown at 23°C under continuous light. The transgenic lines of *A. thaliana* plants (ecotype Colombia-0) used in the present study are listed in Table 1. Original plants expressing GFP-SYP43, TagRFP-VAMP727, CLC2-GFP, and CLC2-mKO were generated as reported previously and obtained from lab stocks (Ebine et al., 2008, 2011; E. Ito et al., 2012; Uemura et al., 2012). The plants expressing VHAa1-GFP and VHAa1-mRFP were kindly provided by Dr. Karin Schumacher (Heidelberg University, Germany). The plants expressing AP1M2-GFP, AP1M2-mRFP, AP2M-GFP, AP4M-GFP, and free-GFP were kindly provided by Dr. Ikuko Hara-Nishimura (Konan University, Japan) and Dr. Tomoo Shimada (Kyoto University, Japan). The transgenic plants expressing combination of the fluorescent protein-tagged proteins of interest were generated by cross-pollination. The GFP used in this study was sGFP.

Plasmid construction. The genomic DNA of *A. thaliana* SYP61 including approximately 2.3 kb of the 5'-upstream sequence and 0.8 kb of the 3'-downstream sequence was PCR-amplified and cloned into the pENTER/D-TOPO entry vector (Thermo Fisher Scientific) to generate SYP61pro:XFP-SYP61. The genomic DNA of *A. thaliana* VAMP721 including approximately 2.0 kb of the 5'-upstream sequence and 0.9 of the kb 3'-downstream sequence was PCR-amplified and cloned as described above to generate VAMP721pro:iRFP-VAMP721. These clones were fused with a cDNA of GFP, mRFP, or iRFP713 (Filonov et al., 2011) using the In-Fusion HD Cloning Kit (Clontech) and then recombined into the destination vector pBGW or pHGW using the Gateway LR

Clonase II enzyme mix (Thermo Fisher Scientific). To generate UBQ10pro:ST-iRFP:NOSter, the DNA corresponding with 52 N-terminal amino acids of a rat 2,6-sialyl transferase (Boevink et al., 1998) was initially PCR-amplified and cloned into the entry vector containing 35S promoter, iRFP, and NOS terminator using In-Fusion HD Cloning Kit (Clontech). The promoter region of the entry vector containing 35Spro:ST:NOSter was subsequently replaced with UBQ10 promoter using In-Fusion HD Cloning Kit (Clontech), and then recombined into the destination vector pBGW using the Gateway LR Clonase II enzyme mix (Thermo Fisher Scientific). For the protoplast transient expression assay, the PCR-amplified cDNA of CLC1, CLC2, or CLC3 was integrated in front of a cDNA encoding GFP or mRFP of binary vectors (modified pBluescript II) with the In-Fusion HD Cloning Kit (Clontech). The GFP-SYP61 vector for protoplast transient expression assay was kindly gifted by Dr. T. Uemura (Uemura et al., 2004). To construct GAL4 AD-fusion vectors for the yeast two-hybrid analysis, the full length coding sequences of large subunits of AP-1 and AP-4 (AP1/2B1: AT4G11380.1, AP1/2B2: AT4G23460, AP1G1: AT1G60070, AP1G2: AT1G23900, AP4B: AT5G11490, AP4E: AT1G31730) were subcloned into pAD-GAL4-GWRFC. To construct GAL4 BD-CHC2 NTD vector, the coding sequence for the amino-terminal domain of CHC2 (residues 1–536) was subcloned into *Sma*I-digested pBD-GAL4-Cam by the In-Fusion reaction. pAD-GAL4-GWRFC was kindy provided by Dr. Taku Demura (Nara Institute of Science and Technology, Japan). BD-RHA1 N123IΔc and AD-VPS9A were gifted from Dr. E. Ito (Goh et al., 2007). The primers used in this study are listed in Table 2.

Conventional confocal laser scanning microscopy (CLSM). The observations were conducted on primary root epidermal cells in the elongation zone of the transgenic seedlings seven days after

germination (7 DAG). Conventional CLSM for 2D (xy) imaging was performed using a Zeiss LSM780 with a Plan-Apochromat 63×/NA 1.4 Oil objective lens, or an α Plan-Apochromat 100×/NA 1.57 Oil-Hi DIC Corr M27 objective lens as the high-resolution objective lens (Carl Zeiss). For visualization of the TGN with lipophilic dye, *Arabidopsis* root cells were treated with 2 μM FM4-64 (Thermo Fisher Scientific). The image of FM4-64 was taken after 6 min of uptake. Fluorescence from GFP, RFP, and FM4-64 was unmixed using linear unmixing algorithms of ZEISS ZEN software. The protoplast transient expression assay was performed as described previously (Ueda et al., 2001; Uemura et al., 2004). Transformed *Arabidopsis* protoplasts were observed with the Zeiss LSM780.

SCLIM and image analyses. I observed the transgenic seedlings 7 DAG as described above. 3D (xyz) and 4D (3D time-lapse) imagings were performed with SCLIM (Kurokawa et al., 2013, 2019, 2020).

---

*The methodology described here has been published in Bio-protocol as an article entitled "Live-cell Imaging by Super-resolution Confocal Live Imaging Microscopy (SCLIM): Simultaneous Three-color and Four-dimensional Live Cell Imaging with High Space and Time Resolution" by Kazuo Kurokawa, and Akihiko Nakano (2020, volume 10, issue 17, e3732. DOI: 10.21769/BioProtoc.3732).

An overview of SCLIM is shown in Figure 1. In brief, it is composed of:

a. Olympus model IX-73 inverted fluorescence microscope with a UPlanSApo 100×/NA 1.4 Oil objective lens (Olympus).

b. Custom-made piezo actuator (Yokogawa Electric). It is equipped to oscillate z-axis position of the objective lens at high frequency (maximum, 30 Hz). I used it at 4 or 8 Hz in this study.

c. Custom-made spinning-disk confocal scanner (Yokogawa Electric).

d. 4× intermediate lens (NIKON, VM lens C-4×), advantageous for raising spatial resolution.

e. Custom-made spectroscopic unit equipped with custom-made dichroic mirrors, reflection mirrors, band pass filters, and a long pass filter to separate 3-color fluorescence (green, red, and infrared) images into 3 different channels. The angles of dichroic mirrors and reflection mirrors can be adjusted from outside of the spectroscopic unit to maintain the quality of SCLIM system.

f. Three image intensifiers (Hamamatsu Photonics). They are cooled with a custom-made cooling system to achieve low signal-to-noise ratio amplification. The amplification gain of each of these 3 image intensifiers is controlled independently.

g. Three EM-CCD cameras (Hamamatsu Photonics, C9100-13) for green, red, and infrared fluorescence channels. They contain 512×512 frame transfer CCD sensor. Pixel size of sensor is 16×16 μm. It corresponds to 0.06×0.06 μm on the sample plane.

h. Three solid-state excitation lasers with emission at 473 nm (Cobolt, CW 473nm, DPSS, 50 mW), 561 nm (Cobolt, CW 561 nm, DPSS, 50 mW), and 671 nm (CrystaLaser, CW 671 nm, DPSS, 100 mW). They can excite green, red, and infrared fluorescent proteins simultaneously. Irradiation of the sample by these 3 lasers is controlled by 3 independent electromagnetic shutters (Sigma Koki). Irradiation powers of these lasers can be adjusted with variable ND

filters.

2D confocal fluorescence data are separated in the custom-made spectroscopic unit. In other words, green, red, and infrared fluorescence pass through the spectral windows defined by two band pass filters (green channel; 490–545 nm and red channel; 580–660 nm) and one long pass filter (infrared channel; 680 nm–). They are simultaneously collected by three EM-CCD cameras at each z-axis position and each time point under the control of a custom-made image acquisition system (Yokogawa Electric).

I routinely assessed and maintained the quality of the SCLIM system (such as evenness of illumination, distortion of the field of view, chromatic lateral shifts, co-localization issues, lateral resolving power, and 3D re-construction precision) with an ARGO-SIM calibration slide (Argolight) (Figure 2). To reduce the effect of chromatic aberration, I used the central region of the field of view (i.e., within a radius of 135 pixels, or 8.1 μm, from the center of the camera) for observations and quantitative analyses in the present study (Figure 2D, dotted circle). In addition, based on the ARGO-SIM calibration slide pattern, I corrected the misalignments in xyz positions in 3 channels using a registration correction function in Volocity (Quorum Technologies). As shown in Figure 2A–K, sub-pixel precision (i.e., less than 60 nm) can be usually seen in the observation area. For 3D observations, I collected 51 optical sections spaced 0.1 μm apart (z-range = 5 μm). For 4D observations, I collected 21 or 31 optical sections spaced 0.1 μm apart, or 16 optical sections spaced 0.2 μm apart (z-range = 2–3 μm). The x and y axis spatial resolution of SCLIM is 180 nm, 180 nm, and 240 nm for green, red, and infrared fluorescence channels, respectively (Figure 2). Z-stack images were reconstructed to 3D images and deconvolved by using theoretical point spread

functions with Volocity (Quorum Technologies). For colocalization analyses, calculations of the Pearson correlation coefficients between the signal intensities of each voxel on the TGN was performed after three-dimensionally segmenting individual TGNs as ROI with Volocity. Thresholds for the calculation of correlation coefficients were automatically determined (Costes et al., 2004). Signal intensity profiles of images were measured with ImageJ as previously reported (Tojima et al., 2019). Whole-mount immunolabelling of *Arabidopsis* roots with the CHC antibody was performed according to previous reports (Boutté & Grebe, 2014; Wattelet-Boyer et al., 2016). The antibodies and dilutions used were as follows: anti-CHC primary antibody (Agrisera, AS10 690; 1/300); AlexaFluor 594-conjugated donkey anti-rabbit IgG secondary antibody (Jackson Immunoresearch, 711-585-152; 1/300).

Electron microscopy. High-pressure freezing/freeze substitution and ultramicrotomy were performed as described previously (Toyooka et al., 2009). In brief, *Arabidopsis* root cells (7 DAG) were frozen in a high-pressure freezer EM-ICE (Leica), substituted/fixed with acetone containing 2% osmium tetroxide. After washing with methanol, the samples were stained with 1% uranyl acetate in methanol and then embedded in epoxy resin. Ultra-thin sections (80 nm) of the fixed sample were mounted on formvar supported 1 hole copper grids and stained with 4% uranyl acetate and lead citrate. Immunoelectron microscopy experiments were performed, as described previously (Toyooka et al., 2009) with some modifications, under the following conditions with 3 antibodies and 3 fixatives. In brief, *Arabidopsis* root cells (7 DAG) expressing either AP1M2-GFP or AP4M-GFP were frozen in a high-pressure freezer EM-ICE (Leica) and substituted/fixed with acetone containing 1% glutaraldehyde (GA), that containing 1% GA and 1% OsO4, or that

containing 0.25% GA and 0.1% uranyl acetate. The fixed samples were then embedded in LR White resin. Ultrathin sections of the sample were labeled with anti-GFP primary antibodies (Invitrogen A11122: 1/200 for 1h, 1/200 for 3h, or 1/50 for 1h; or Abcam ab290: 1/50 for 1h; or Roche: 1/100 for 2h or 1/500 for 1h; or mix of 1/200 Invitrogen and 1/50 Abcam for 1h). The samples were acquired with a transmission electron microscope JEM-1400 Flash (JEOL).

Yeast two-hybrid analysis. The pAD and pBD vectors were transformed into *S. cerevisiae* strain AH109 (Clontech, Takara Bio) with a polyethylene glycol/lithium acetate protocol. The transformants with both vectors were grown on the solid synthetic dextrose medium lacking Leu and Trp. To examine interactions between the pAD- and pBD-fusion proteins, the transformants were grown on the solid synthetic dextrose medium lacking Leu, Trp, His, and adenine for 4 d at 30°C. AD-RHA1 N123IΔc and BD-VPS9A were used for the control experiment (Goh et al., 2007). Empty vectors, pAD-GAL4-2.1 and pBD-GAL4-Cam, were used as negative controls. Five independent colonies were tested for each interaction.

Coimmunoprecipitation analysis. A coimmunoprecipitation analysis was performed according to the case of AP2M (Yamaoka et al., 2013). In brief, approximately 0.4 g of *A. thaliana* expressing AP1M2-GFP, AP4M-GFP, AP2M-GFP, or free-GFP (14 DAG) were homogenized on ice in 1.2 mL of a lysis buffer (50 mM Tris-HCl, pH7.5, 1 mM EDTA, 1% Triton X-100, and protease inhibitor cocktail in the absence of NaCl) and then centrifuged at 10,000g for 10 min at 4°C. The supernatants were immunoprecipitated with an anti-GFP antibody using μMACS GFP Isolation Kit (Miltenyi Biotec). Then, the immunoprecipitates were separated by SDS-PAGE and immunoblotted with an

anti-GFP antibody (Clontech, No. 632375; 1/20,000) or an anti-CHC antibody (Agrisera, AS10 690; 1/2,000). Anti-Mouse IgG, HRP-Linked Whole Ab Sheep (GE Healthcare, NA931; 1/5,000) and Anti-Rabbit IgG, HRP-Linked Whole Ab Donkey (GE Healthcare, NA934; 1/5,000) secondary antibodies were used to detect the primary antibodies with ECL select western blotting detection reagent (RPN2235, GE Healthcare). Densitometry was performed with "Quantification of Gel Bands by an Image J Macro, Band/Peak Quantification Tool (Ohgane, 2019)". The band intensities of CHC were divided by the band intensity of each corresponding GFP-tag, normalized to the AP1M2-GFP line, and expressed as the relative co-immunoprecipitated CHC.

Statistics. Sample sizes were at least 30 TGNs from at least 3 individual plants for colocalization analyses on a TGN. Statistical analyses were performed with R version 3.3.1. Two-sided Steel-Dwass test was used for multiple comparisons. Two-sided Wilcoxon rank-sum test was used for two-group comparisons. *P* values less than 0.01 were considered as statistically significant.

Table 1. The plant lines used in this study.

Name	Background	Complementation	Source
SYP61pro:GFP-SYP61	Wild type, ecotype Columbia	✓	This study
SYP61pro:mRFP-SYP61	Wild type, ecotype Columbia	Not-tested	This study
SYP61pro:iRFP-SYP61	Wild type, ecotype Columbia	Not-tested	This study
SYP43pro:GFP-SYP43	*syp43* mutant, ecotype Columbia (SALK_144268)	✓	Uemura et al. (2012)
VHAa1pro:VHAa1-GFP	Wild type, ecotype Columbia	Not-tested	Dettmer et al. (2006)
VHAa1pro:VHAa1-mRFP	Wild type, ecotype Columbia	Not-tested	Viotti et al. (2010)
AP1M2pro:AP1M2-GFP	Wild type, ecotype Columbia	✓*	Teh et al. (2013)
AP1M2pro:AP1M2-mRFP	Wild type, ecotype Columbia	Not-tested	Fuji et al. (2016)
AP2Mpro:AP2M-GFP	*ap2m* mutant, ecotype Columbia (SAIL_165A05)	✓	Yamaoka et al. (2013)
AP4Mpro:AP4M-GFP	*ap4m* mutant, ecotype Columbia (SALK_044748)	✓	Fuji et al. (2016)
VAMP721pro:iRFP-VAMP721	Wild type, ecotype Columbia	Not-tested	This study
VAMP727pro:TagRFP-VAMP727	Wild type, ecotype Columbia	Not-tested	Ebine et al. (2008)
CLC2pro:CLC2-GFP	Wild type, ecotype Columbia	Not-tested	Ebine et al. (2011)
CLC2pro:CLC2-mKO	Wild type, ecotype Columbia	Not-tested	E. Ito et al. (2012)
Free-GFP (CaMV 35S:sGFP-BE:NOSter)	Wild type, ecotype Columbia	—	Mano et al. (1999)
UBQ10pro:ST-iRFP:NOSter	Wild type, ecotype Columbia	—	This study

Check marks (✓) indicate that the functionality was verified as normal in complementation tests.
*The complementation test for AP1M2-GFP was conducted in Wassilewskija ecotype (FLAG_293C11).

Table 2. The list of primers used for plasmid construction in this study.

Name	Sequence	Purpose
promoter_GFP_SYP61_1	CACCGTTACGTAAGGATGTGCGTCACAGGAA	For construction of SYP61pro:xFP-SYP61
promoter_GFP_SYP61_2	CCTTGTGTGTATCTGACCTGTGCGTTT	For construction of SYP61pro:xFP-SYP61
promoter_GFP_SYP61_3	AAAATTTTGTTGATTTCGGGATGGTGAGCAAGGGCGAGGAGCTGT	For construction of SYP61pro:GFP-SYP61
promoter_GFP_SYP61_4	TCCTCGCCCTTGCTCACCATCCCGAAATCAACAAAATTTTGCTAC	For construction of SYP61pro:GFP-SYP61
promoter_GFP_SYP61_5	TGTACAAGGGAGGTAGTGGCATGTCTTCAGCTCAAGATCC	For construction of SYP61pro:GFP-SYP61
promoter_GFP_SYP61_6	GAAGACATGCCACTACCTCCCTTGTACAGCTCGTCCATGCCGTGA	For construction of SYP61pro:GFP-SYP61
infusion_RFP-SYP61_promoter	CTCGGAGGAGGCCATCCCGAAATCAACAAAATTTTGCTAC	For construction of SYP61pro:mRFP-SYP61
infusion_RFP-SYP61_ORF	GGAGGTAGTGGCATGTCTTCAGCTCAAGATCCATTCT	For construction of SYP61pro:mRFP-SYP61
infusion_iRFP-SYP61_promoter	GGATCCTTCAGCCATCCCGAAATCAACAAAATTTTGCTAC	For construction of SYP61pro:iRFP-SYP61
infusion_iRFP-SYP61_ORF	GGAGGTAGTGGCATGTCTTCAGCTCAAGATCCATTCT	For construction of SYP61pro:iRFP-SYP61
iRFP Bam-f.	ATGGCTGAAGGTTCCGTCGC	For construction of VAMP721pro:iRFP-VAMP721
iRFP-linker r.	GCCACTACCTCCTCCCTCTTCCATCACGCCGATCT	For construction of VAMP721pro:iRFP-VAMP721
linker-VAMP721 f.	GGAGGTAGTGGCGGCATGGCGCAACAATCGTTGAT	For construction of VAMP721pro:iRFP-VAMP721
pVAMP721-iRFP-r.	GGAACCTTCAGCCATTTTTTCTTTACCTTAAATCT	For construction of VAMP721pro:iRFP-VAMP721
p35S-Bam r.	GGATCCCGTGTTCTCT	For construction of 35Spro:ST-iRFP:NOSter
iRFP Bam-f.	ATGGCTGAAGGTTCCGTCGC	For construction of 35Spro:ST-iRFP:NOSter
p35S-Bam-ST f.	AGAGAACACGGGATCCATGATTCATACCAACTTG	For construction of 35Spro:ST-iRFP:NOSter
ST-Bam-iRFP-r.	CCTTCAGCCATGGATCCCATGGCCACTTTCTCCTG	For construction of 35Spro:ST-iRFP:NOSter
pUBQ10-Bam-ST-f	TTAACAGGGATCCATGATTCATACCAACTTGAAG	For construction of UBQ10pro:ST-iRFP:NOSter
pBS MCS r.	GAATTCCTGCAGCCCGGG	For construction of UBQ10pro:ST-iRFP:NOSter
pBS-EcoRI-pUBQ10 f.	GGGCTGCAGGAATTCGTTGTCGACGAGTCAGTAAT	For construction of UBQ10pro:ST-iRFP:NOSter
pUBQ10-Bam-R	ATGGATCCCTGTTAATCAGAAAAACTCA	For construction of UBQ10pro:ST-iRFP:NOSter
pBSⅡ/CLC1 Infusion_F	TTGGAGAGGGGGATCCATGGCGACTTTTGATGATGG	For construction of 35Spro:CLC1-xFP:NOSter
pBSⅡ/CLC1-GFP Infusion_R	TGCTCACCATGGATCCCTCCGCCTTGGTTCCCTC	For construction of 35Spro:CLC1-GFP:NOSter
pBSⅡKS+/CLC1-mRFP Infusion_R	AGGAGGCCATGGATCCCTCCGCCTTGGTTCCCTC	For construction of 35Spro:CLC1-mRFP:NOSter
pBSⅡ/CLC2 Infusion_F	TTGGAGAGGGGGATCCATGTCTGCCTTTGAAGACG	For construction of 35Spro:CLC2-xFP:NOSter
pBSⅡ/CLC2-GFP Infusion_R	TGCTCACCATGGATCCAGCAGCAGTAACTGCCTC	For construction of 35Spro:CLC2-GFP:NOSter
pBSⅡKS+/CLC2-mRFP Infusion_R	AGGAGGCCATGGATCCAGCAGCAGTAACTGCCTC	For construction of 35Spro:CLC2-mRFP:NOSter
pBSⅡ/CLC3 Infusion_F	TTGGAGAGGGGGATCCATGTCGTCAACCTTGAGCA	For construction of 35Spro:CLC3-xFP:NOSter
pBSⅡ/CLC3-GFP Infusion_R	TGCTCACCATGGATCCCAACTTCTCTGTAACTGTGA	For construction of 35Spro:CLC3-GFP:NOSter
pBSⅡKS+/CLC3-mRFP Infusion_R	AGGAGGCCATGGATCCCAACTTCTCTGTAACTGTGA	For construction of 35Spro:CLC3-mRFP:NOSter
pBD_CHC2_Infusion-F	CGCCGGAATTCGCCCTAATGGCGGCTGCCAACGCCCCCAT	For construction of pBD-GAL4/CHC2 NTD
pBD_CHC2_1-536_Insusion-R	CTCTAGAGTCGACCCTTAACGGAGTATGGTTTGCAGAAG	For construction of pBD-GAL4/CHC2 NTD
AP1B1_Y2H_pENTR-F	CACCATGAGTGGTCACGATTCGAA	For construction of pAD-GAL4/AP1B1
AP1B1_Y2H_pENTR-R	TCAAGCCTTGAAGAGAAGCTCC	For construction of pAD-GAL4/AP1B1
AP1B2_Y2H_pENTR-F	CACCATGAGCGGTCATGATTCTAA	For construction of pAD-GAL4/AP1B2
AP1B2_Y2H_pENTR-R	TCAAGCCTTGAAGAGAATTTCG	For construction of pAD-GAL4/AP1B2
AP1G1_Y2H_pENTR-F	CACCATGAATCCATTCTCTTCCGG	For construction of pAD-GAL4/AP1G1
AP1G1_Y2H_pENTR-R	TCATAACCCACGTGGGAAA	For construction of pAD-GAL4/AP1G1
AP1G2_Y2H_pENTR-F	CACCATGAATCCCTTTTCTTCTGG	For construction of pAD-GAL4/AP1G2
AP1G2_Y2H_pENTR-R	TCACAACCCGCGAGGGAAGTTG	For construction of pAD-GAL4/AP1G2
AP4B_Y2H_pENTR-F	CACCATGGCTCCTCCGGCCGCTT	For construction of pAD-GAL4/AP4B
AP4B_Y2H_pENTR-R	TTAGTAACACAACGAAACGAAATC	For construction of pAD-GAL4/AP4B
AP4E_Y2H_pENTR-F	CACCATGGAGCAGCTAAAGACAATTGG	For construction of pAD-GAL4/AP4E
AP4E_Y2H_pENTR-R	CTAGCCGAGGAGATCTTTG	For construction of pAD-GAL4/AP4E

Chapter 3: Results

Different distributions of V-ATPase and SNAREs on the TGN

SYP4 family proteins (SYP41, 42, and 43) and SYP61 have been studied as well-established TGN markers (Bassham et al., 2000; Sanderfoot et al., 2001). In addition, a subtype of V-ATPase is also known to reside at the TGN (Dettmer et al., 2006). VHAa1 is an integral membrane protein subunit of the TGN-resident V-ATPase, which is essential for pH homeostasis of the TGN lumen (Nishi & Forgac, 2002). To better understand the relationship between these TGN markers, I compared the distribution of these proteins with fluorescent tags on the TGN by conventional confocal laser scanning microscopy (CLSM) and SCLIM. They showed punctate patterns in 2D (CLSM) and round or ellipsoid shapes in 3D (SCLIM) (Figure 3). GFP-SYP43, mRFP-SYP61 and VHAa1-mRFP almost completely colocalized with each other by conventional CLSM as well as the control colocalization between GFP-SYP61 and mRFP-SYP61 (Figure 3A–C). By SCLIM, GFP-SYP43 and mRFP-SYP61 also showed good colocalization like the control GFP-SYP61 vs mRFP-SYP61 (Figure 3D and E). However, GFP-SYP43 and VHAa1-mRFP were significantly segregated when observed by SCLIM (Figure 3F). To quantitatively evaluate the colocalization, I calculated the correlation between GFP and RFP signal intensities per voxel on the TGN. The resulting number of this calculation reflects the degree of overlap of the molecules with 1 representing a complete overlap, and 0 indicating a random distribution. The results confirmed that the extent of colocalization was significantly low for SYP43 and VHAa1 (Figure 3G), indicating that TGN-localized proteins with different functions are not uniformly distributed in the same TGN. By comparison with the location of *trans*-Golgi cisternae marked with ST-iRFP (infrared fluorescent protein-tagged *trans*-membrane domain of a rat sialyl transferase (Boevink et al., 1998)), I examined whether SYP43 and VHAa1 show any biased

localization along the proximal–distal axis of the TGN, but could not observe a clear tendency (Figure 4).

Secretory- and vacuolar-trafficking zones in the TGN defined by R-SNAREs

R-SNAREs play a role in guiding vesicles to target membranes where cognate Q-SNAREs are present (Lipka et al., 2007; Saito & Ueda, 2009; Staehelin & Moore, 1995). R-SNAREs are sorted into vesicles together with non-SNARE cargo proteins in the donor compartment, although the mechanisms for interaction with coat proteins are different (Miller et al., 2007, 2011; Pryor et al., 2008). Among the R-SNAREs that reside at the TGN, I decided to examine the behaviors of VAMP721 and VAMP727. As described in the chapter 1, these proteins are known to travel different routes after they leave the TGN, to the PM and to the vacuole, respectively (Ebine et al., 2008; El Kasmi et al., 2013; Kwon et al., 2008; Uemura et al., 2019; Zhang et al., 2011). I established *Arabidopsis* plants expressing iRFP-VAMP721 (iRFP-tagged VAMP721), TagRFP-VAMP727 (TagRFP-tagged VAMP727), and GFP-SYP61, and performed three-color 3D observation by SCLIM. As shown in Figure 5A and B, iRFP-VAMP721 and TagRFP-VAMP727 localized to distinct regions of the same TGN labeled with GFP-SYP61. Similar results were obtained in comparison to another TGN marker, VHAa1 (Figure 5C and D). Hereafter I call these TGN subregions “zones.” The clear segregation of VAMP721 and VAMP727 on the TGN suggests that the TGN has spatially distinct zones for “secretory trafficking” to the PM and for “vacuolar trafficking.” As a control, I compared localizations of GFP-, mRFP- and iRFP-tagged SYP61 (Figure 6). They overlapped very well with each other, indicating neither different effects of different fluorescent tags nor chromatic aberrations were causing positional shifts of fluorescent signals.

AP-1 and AP-4 are located in secretory- and vacuolar-trafficking zones in the TGN, respectively

To investigate whether these trafficking zones labeled with the two R-SNAREs are responsible for cargo sorting, I next focused my attention on the adaptor protein complexes AP-1 and AP-4. The plant AP-1 and AP-4 have been reported to colocalize with TGN markers but not with each other by Shimada and Hara-Nishimura's research group (Fuji et al., 2016; Teh et al., 2013).

First, to investigate the involvement of AP-1 and AP-4 in secretory trafficking, I performed SCLIM observation of *Arabidopsis* plants expressing iRFP-VAMP721, AP1M2 (μ-subunit of AP-1)-mRFP, and AP4M (μ-subunit of AP-4)-GFP. As shown in Figure 7, AP4M-GFP did not colocalize with either AP1M2-mRFP or iRFP-VAMP721, whereas AP1M2-mRFP and iRFP-VAMP721 colocalized well. This result strongly suggests that the AP-1 complex is in the secretory-trafficking zone of the TGN.

Next, to examine the roles of AP-1 and AP-4 in the vacuolar-trafficking zone, I generated *Arabidopsis* plants expressing either AP1M2-GFP or AP4M-GFP in addition to TagRFP-VAMP727 and iRFP-SYP61 and performed SCLIM observation. As shown in Figure 8, TagRFP-VAMP727 showed partial colocalization with AP4M-GFP but not with AP1M2-GFP. It should be noted that TagRFP-VAMP727 without the iRFP-SYP61 signal, which probably represent VAMP727 in multivesicular endosomes, did not colocalize with either AP1M2-GFP or AP4M-GFP (Figure 8, arrowheads). Taken together, these results suggest that AP-4 is present in the vacuolar-trafficking zone of the TGN. In addition, the majority (approximately 85%) of AP1M2-mRFP and AP4M-GFP localized on distinct zones of the same TGN labeled with iRFP-SYP61 (Figure 9A–D) and/or

FM4-64 (lipophilic dye) (Figure 9E–G). To investigate the structural details of the TGN zones labeled with either AP-1 or AP-4, I also tried to perform immunoelectron microscopy experiments under the various conditions with 3 antibodies and 3 fixatives. However, to my disappointment, I was not able to claim confidently that a zone of the TGN was specifically immunolabeled, although I sometimes saw images, in which a part of the TGN appeared to have immunogold signals (Figure 10). The low reproducibility was most probably due to very small amounts of antigens under my experimental conditions.

Clathrin is present in the secretory-trafficking zone of the TGN

Clathrin is a coat protein to shape membranes to form CCVs, which are major carriers of cargo proteins at the PM and the TGN. (D. G. Robinson & Pimpl, 2014) The AP complexes, AP-1 and AP-2, are known to interact with clathrin (Hirst et al., 2011; Keen, 1987). As compared to the well-characterized dynamics of clathrin/AP-2-mediated endocytosis (Bashline et al., 2013; Di Rubbo et al., 2013; Kim et al., 2013; McMahon & Boucrot, 2011; Yamaoka et al., 2013), the behavior of CCVs formed at the TGN remains largely unknown in plant cells. The previous study by using conventional CLSM showed that fluorescent protein-tagged clathrin, CLC2-mKO (monomeric Kusabira Orange-tagged clathrin light chain 2) localized largely to the TGN, while its substantial portion was also found in the close proximity of the Golgi apparatus (E. Ito et al., 2012). To gain an insight into more precise localization of clathrin in the Golgi/TGN region, I generated *Arabidopsis* plants expressing ST-iRFP, GFP-SYP61, and CLC2-mKO, and observed them by SCLIM. Consistent with the previous study (Uemura et al., 2014), many TGNs labeled with GFP-SYP61 were found adjacent to the Golgi apparatus labeled with ST-iRFP (Figure 11). CLC2-mKO partially

overlapped with GFP-SYP61 (TGN) and located on the opposite side to ST-iRFP (*trans*-Golgi), suggesting that clathrin accumulated on the distal side of the TGN membrane (Figure 11).

I next generated *Arabidopsis* plants expressing AP1M2-GFP or AP4M-GFP in addition to CLC2-mKO. SCLIM observation showed that AP1M2-GFP colocalized well with CLC2-mKO (Figure 12A), but AP4M-GFP did not (Figure 12B). The quantitative colocalization analyses showed that AP-1 has significantly high degree of colocalization with clathrin as compared to AP-4 (Figure 12C).

It should be noted that *A. thaliana* has three CLC isoforms (CLC1–3) and two clathrin heavy chain (CHC) isoforms (CHC1 and CHC2) (Chen et al., 2011). Considering a possibility that different isoforms of clathrin may reside in different subpopulations of clathrin-coated structures, I compared the localization of fluorescent protein-tagged CLC1, CLC2, and CLC3 in *Arabidopsis* protoplasts. They colocalized with the TGN puncta (Figure 13A–C) and showed very close localization to each other, indicating that their properties are similar at least for the subcellular localization (Figure 13D–F). I also observed the subcellular localization of endogenous CHCs by whole-mount immunofluorescence staining with the anti-CHC antibody that recognizes both CHC isoforms of *A. thaliana* (Agrisera, AS10 690). The immunostaining images showed that endogenous CHCs highly colocalized with CLC2-GFP and AP1M2-GFP but not with AP4M-GFP (Figure 14). Taken together, these results suggest that clathrin mainly localizes to the secretory-trafficking zone of the TGN.

I next examined the protein interaction of AP-1 and AP-4 with clathrin by yeast two-hybrid and co-immunoprecipitation analyses. Since the large subunits of AP-1–3 have been shown to bind the amino-terminal domain of CHC in mammalian systems (Dell'Angelica, 2001;

Lemmon & Traub, 2012), I compared the interaction between large subunits of AP-1 and AP-4 vs the amino-terminal domain of CHC2 by the yeast two-hybrid analysis. As shown in Figure 15, AP1G1 and AP1G2 (γ subunits of AP-1) but not AP1B1 or AP1B2 (β subunits of AP-1) interacted strongly with the amino-terminal domain of CHC2. The interaction of CHC2 amino-terminal domain was not detected with either AP4B (β subunit of AP-4) or AP4E (ε subunit of AP-4). I also investigated the interaction by the co-immunoprecipitation analysis using *Arabidopsis* plants expressing either AP1M2-GFP, AP4M-GFP, AP2M-GFP (positive control; Yamaoka et al., 2013), or free-GFP (negative control) with antibodies against GFP or CHCs. The results (Figure 16A and B) showed that the anti-GFP brought down a significant amount of CHC when AP1M2-GFP was expressed but much less when AP4M-GFP was expressed (see lanes no. 13 and 14). The biochemical evidence for the interaction of plant AP-1 with clathrin has been shown in the previous study (Park et al., 2013), and my results are consistent with this finding. It is notable that a small amount of CHC was also detected in the anti-GFP immunoprecipitates from AP4M-GFP-explessing plants (quantification is shown in Figure 16B). These results indicate that clathrin is indeed present in the secretory-trafficking zone of the TGN represented by AP-1, although the involvement of a small portion of clathrin in the vacuolar-trafficking zone marked by AP-4 cannot be ruled out.

Temporal dynamics of the secretory- and vacuolar-trafficking zones of the TGN

Having revealed spatial features of the TGN zones by 3D imaging, I next investigated their temporal dynamics by 4D imaging. First, *Arabidopsis* plants expressing iRFP-SYP61, AP1M2-mRFP and AP4M-GFP as markers of the TGN, the secretory-trafficking zone, and the vacuolar-trafficking zone, respectively, were subjected to 4D imaging analysis by the simultaneous 3-color, high-resolution and

high-speed SCLIM observation. As shown in Figure 17, I frequently observed budding of the AP1M2-mRFP signal from the TGN without AP4M-GFP as structures approximately 500 nm in diameter (arrowheads). I also noticed that portions of iRFP-SYP61 left together with AP1M2-mRFP sometimes (Figure 17). Contrary to my expectation, the budding of AP4M-GFP from the TGN was not seen during my observations. From these results, I concluded that the zones for secretory trafficking and vacuolar trafficking are not only spatially distinct but also have different dynamics.

Next, I examined the dynamics of AP-1, AP-4, and VAMP721 by the simultaneous SCLIM observation. *Arabidopsis* plants expressing iRFP-VAMP721, AP1M2-mRFP, and AP4M-GFP showed that AP1M2-mRFP and iRFP-VAMP721 behaved together and simultaneously left the TGN labeled with the 3-color fluorescence (Figure 18, arrowheads). On the other hand, AP4M-GFP behaved independently from both iRFP-VAMP721 and AP1M2-mRFP (Figure 18). These results suggest that the AP-1 and VAMP721 function coordinately in the same secretory-trafficking pathway. Furthermore, a small punctum containing AP1M2-mRFP and iRFP-VAMP721 (arrows) separated from the TGN-detached structure with the dual-color fluorescence (arrowheads) (Figure 18).

I further examined the temporal relationship between AP-1, AP-4 and clathrin. 4D imaging of AP1M2-GFP or AP4M-GFP and CLC2-mKO showed that CLC2-mKO always behaved together with AP1M2-mRFP (Figure 19A and C). In contrast, the movement of CLC2-mKO occurred independently from AP4M-GFP (Figure 19B and D). These observations support the idea that clathrin functions in the secretory-trafficking zone, but not in the vacuolar-trafficking zone.

Portions of the secretory-trafficking zone become fragmented after budding from the TGN

To investigate the temporal dynamics of the secretory-trafficking zone component clathrin in relation to the Golgi and the TGN, I performed 4D imaging for *Arabidopsis* plants expressing ST-iRFP, GFP-SYP61, and CLC2-mKO. In Figure 20, the TGN labeled with GFP-SYP61 at time 0 s was adjacent to the Golgi apparatus labeled with ST-iRFP (Figure 20A, 0 s). Some research groups have recently reported that the plant TGN shows two different forms; the Golgi-associated TGN (GA-TGN) and the free TGN (also called the Golgi-released independent TGN; GI-TGN) (Kang et al., 2011; Staehelin & Kang, 2008; Uemura et al., 2014, 2019; Viotti et al., 2010). The former is the typical TGN, which is adjacent to the *trans*-cisterna of the Golgi apparatus. The latter is the novel type of the TGN and originates from the GA-TGN, which does not associate with the Golgi apparatus. The TGN of Figure 20A, 0 s, was clearly the GA-TGN. A part of the TGN marked by GFP-SYP61 was then detached as a new free TGN (Figure 20A, 6.4-25.6 s, arrowheads). Interestingly, CLC2-mKO separated from the GA-TGN together with the newly formed free TGN and stayed with free TGN for some period of time (Figure 20A, arrowheads and squares). The size of this CLC2-mKO signal was approximately 500 nm in diameter, which was similar to that of the budding AP-1 signals from the TGN shown in Figure 17. Such a large size is much bigger than that of CCVs, with an average diameter of 60 nm, reported by electron tomography in plant cells (Narasimhan et al., 2020) and PM-localized CLC2-mKO fluorescence equivalent to clathrin-coated pits (Figure 21). As shown in Figure 20A (32.0 s and later)–C, the GFP-SYP61 and CLC2-mKO signals eventually split and fragmented into distinct small structures. I also investigated the ultrastructure of the TGN by transmission electron microscopy. *Arabidopsis* root cells were fixed by high-pressure freezing/freeze substitution, and ultrathin sections were prepared. As shown in Figure 22, the free TGN, which is distinguished by the structure and the presence of clathrin, appeared to be

composed of multiple vesicles/buds including clathrin-coated profiles and sometimes a cluster of CCVs was found near the Golgi/TGN. These results suggest that free TGN forms a structure containing a cluster of vesicles/buds, some of which have clathrin profiles. After leaving from Golgi, this structure may well get fragmented into separate vesicles. I also noticed that the CLC2-mKO fluorescence often increased on the GA-TGN before budding, perhaps reflecting gradual accumulation of clathrin on the GA-TGN membrane in advance of the release of the free TGN/vesicle cluster (Figure 23).

Chapter 4: Discussion

It is widely accepted that the TGN plays a pivotal role as the protein-sorting platform for post-Golgi trafficking. Proteins with a variety of destinations are sorted there from each other and then further delivered to their final locations. To understand molecular mechanisms how they find correct carriers and paths, cutting-edge live imaging is deemed a powerful approach. However, the style of presence of the TGN is complicated and differs among species. The TGN is often associated with the Golgi complex and thus used to be regarded as a part of the Golgi apparatus, but emerging evidence indicates that the TGN can function independently of the Golgi. Plant cells have notable advantages for studying the functions and the dynamics of the TGN in this regard. First, considering the structure of the Golgi apparatus, plant cells show beautifully stacked Golgi cisternae, which are separate as ministacks in the cytoplasm (Kang et al., 2011; Staehelin & Kang, 2008), unlike in mammalian cells where they form a huge Golgi ribbon (Klumperman, 2011) and yeast *Saccharomyces cerevisiae* cells where unstacked cisternae are scattered in the cytoplasm (Kurokawa et al., 2019; Tojima et al., 2019). Another important feature of plant cells is the clear evidence showing the dynamic nature of the TGN. Not only does the TGN associate with the Golgi (GA-TGN), but it can also behave independently from the Golgi (free TGN/GI-TGN) (Kang et al., 2011; Staehelin & Kang, 2008; Uemura et al., 2014, 2019; Viotti et al., 2010). Uemura and colleagues have previously demonstrated by SCLIM that the free TGN/GI-TGN forms from the GA-TGN (Uemura et al., 2014, 2019). This kind of separation of the TGN from the main body of the Golgi apparatus is also seen in mammalian cells and Drosophila (Fujii et al., 2020; T. Tojima and A. Nakano, unpublished) and, in *S. cerevisiae*, as well (Kurokawa et al., 2019; Tojima et al., 2019).

In the present study, I decided to apply the high-performance live imaging microscopy

SCLIM to visualize the events during protein sorting at the TGN in plant cells. I chose Q-SNAREs, SYP43 and SYP61, and a V-ATPase subunit VHAa1 as TGN markers, and examined the behaviors of R-SNAREs, VAMP721 and VAMP727, as cargo proteins destined for secretory and vacuolar trafficking, respectively. Important players involved in sorting, adaptor complexes, AP-1 and AP-4, as well as clathrin, were also visualized and analyzed.

First, I demonstrated that SCLIM indeed had high space-resolution as compared to conventional CLSM. SCLIM observation showed that the TGN markers SYP43 and SYP61 highly colocalized but had a slightly different localization from VHAa1. Such difference was not showed by conventional CLSM (Figure 3). Next, I found that VAMP721 and VAMP727 showed clearly segregated localizations within the same TGN (Figure 5), suggesting that these localizations represent distinct zones in the TGN. Simultaneous observation of SYP61, VAMP721 and VAMP727 together with AP-1 and AP-4 indicated that VAMP721 vs AP-1 and VAMP727 vs AP-4 had high degrees of colocalization as compared to other combinations. This finding supports the notion that AP-1 is involved in the sorting of VAMP721, which is destined to be transported to the PM, whereas AP-4 has a role in the sorting of VAMP727, which is to be transported to the vacuole (Figure 7 and 8). AP-1 and AP-4 were also clearly segregated from each other (Figure 9), again indicating that they represent distinct zones within the TGN corresponding to the two different trafficking paths (Figure 24). Interestingly, clathrin, which was located on the distal side of the TGN, showed very high degree of colocalization with AP-1 but not with AP-4. It should be noted that the segregation of SYP43 and VHAa1 described above was not as distinct as that of AP-1 and AP-4 (compare Figure 3G and Figure 5C; median of colocalization correlation coefficient = 0.72 and 0.50, respectively). The reason for low colocalization of SYP43 and VHAa1 with overlapping residence is unknown at

present.

Evolutionary diversification of APs is an interesting topic and has been discussed in several recent articles. Despite their structural conservation, however, functional similarities between different species are not well understood. My present study provides clear visual demonstration that two of them, plant AP-1 and AP-4, function in two distinct sorting events in the TGN for secretory and vacuolar trafficking, respectively, and localize to two distinct zones in the same TGN.

Several lines of evidence already exist to support the roles of VAMP721 and AP-1 in secretory trafficking (El Kasmi et al., 2013; Kwon et al., 2008; Park et al., 2013; Shimada et al., 2018; J.-G. Wang et al., 2013; Zhang et al., 2011). VAMP721 (and its close paralog VAMP722) has been shown to form a PM SNARE complex with PEN1/SYP121 (Qa) and SNAP33 (Qb+Qc) and cytokinesis-specific SNARE complexes, one with KNOLLE/SYP111 (Qa) and SNAP33 (Qb/c) and another with KNOLLE/SYP111 (Qa), NPSN11 (Qb), and SYP71 (Qc), for secretory trafficking (El Kasmi et al., 2013; Kwon et al., 2008). *vamp721 vamp722* double mutant seedlings exhibit defects in the secretory trafficking of PM-resident LTI6a/RCI2a and PIP2A/PIP2;1 (Zhang et al., 2011). *ap1* mutants show defects in the secretory and recycling trafficking of invertase, secGFP, mucilage, BRASSINOSTEROID INSENSITIVE1, and auxin efflux carrier PIN2 to the PM (Park et al., 2013; Shimada et al., 2018; J.-G. Wang et al., 2013). *vamp721vamp722* double mutant and *ap1* mutant seedlings also exhibit incomplete cell plate formation and abnormal localization of Qa-SNARE KNOLLE/SYP111 (El Kasmi et al., 2013; Park et al., 2013; Teh et al., 2013; Zhang et al., 2011). The observations made in the present study, which showed not only the colocalization but also the synchronized dynamics of VAMP721 and AP-1, provide the first concrete visualization of how they cooperate during the sorting for the trafficking in a unique zone of the TGN. It should be noted here

that the cooperation of VAMP721 and AP-1 as well as clathrin continues even after the TGN separates from the Golgi to become the free TGN. In the electron-microscopic observation shown in Figure 22, the free TGN appears to contain multiple vesicles/buds, as reported before in other plant cell lines, such as *Arabidopsis* hypocotyl and tobacco BY-2 cells (Kang et al., 2011; Staehelin & Kang, 2008; Toyooka et al., 2009). It may well be fragmented into separate vesicles at a later stage. The fate of individual vesicles after fragmentation is an interesting topic for future research.

Interestingly, in contrast to the dynamic behavior of AP-1, AP-4 appears to persist on the GA-TGN for a longer period of time. The mechanism of AP-4-mediated protein transport remains elusive, but *ap-4* mutants showed defects in the vacuolar sorting of soluble vacuolar cargo proteins, such as 12S globulin and CT24 (Fuji et al., 2016; Müdsam et al., 2018). In addition, AP4M was shown to bind to VACUOLAR SORTING RECEPTORs (Fuji et al., 2016; Gershlick et al., 2014), indicating that AP-4 mediates vacuolar trafficking. Considering that VAMP727 and VACUOLAR SORTING RECEPTORSs localize to the multivesicular endosome as well as the TGN, AP-4 probably mediates the trafficking from the TGN to the multivesicular endosome. Unlike AP-1, AP-4 was found to not be associated with clathrin in SCLIM observations. Nevertheless, a small quantity of clathrin was co-immunoprecipitated with AP-4 (Figure 16). This might be explained from the point of view of their evolution. AP complexes have evolved from a common ancestor. Phylogenetic analysis of AP complexes revealed that AP-5 diverged first, followed by AP-3 and then AP-4. AP-1 and AP-2 diverged most recently with the ability to interact with clathrin (Dacks & Robinson, 2017). Thus, AP-4 might have the potential to interact with clathrin. However, even so, the competition to interact with clathrin between AP-1 and AP-4 would occur, leading to the binding of significant amount clathrin with AP-1 rather than with AP-4. Some clathrin-binding motifs have been shown to

competitively bind to the amino-terminal domain of CHC (Doray & Kornfeld, 2001; Teo et al., 2001). The yeast two-hybrid and Co-IP analyses presented here support that AP-1 binds stronger with clathrin than AP-4. Whether VAMP727 is released from the TGN in the form of vesicles or delivered to the vacuolar path by maturation-type or organelle-contact processes remains to be addressed. Further studies of cargo transport between the TGN and the multivesicular endosome will provide more insights into the vacuolar trafficking.

Here, I firstly demonstrated that the single TGN has the distinct trafficking zones for the secretory- and vacuolar-trafficking in living *Arabidopsis* plants by triple-color imaging. Such a zone-type sorting fashion may also be conserved in other organisms. Nakano and colleagues recently revealed that different cargo adaptors, such as AP-1, AP-3, and GGA2, exhibit spatiotemporally distinct assembly patterns, similarly to the zones observed in this study, in *S. cerevisiae* by two-color SCLIM (Tojima et al., 2019). Yuson Guo and colleagues also reported cargo adaptors, such as AP-1, AP-3, GGA2, and epsinR, showed distinct spatial localizatino in mammalian culture cells using two-color stochastic optical reconstruction microscope (Huang et al., 2019). Thus, the concept of sorting zones in the TGN is consistent with the previous reports. Further investigations in other organisms and cell lines will be important to explore the generality of these findings. On the other hand, the question how these trafficking zones are generated remains astill unaddressed. One possible mechanism in plant cells is ECHIDNA (ECH)-dependent protein recruitment at the TGN. ECH, an ortholog of the yeast TVP23 (Tlg2/orthologs of SYP4s-Vesicle Protein 23), is essential for proper localization of the TGN-resident proteins, such as VHAa1, SYP61, RABA2a, ADP-ribosylation factor 1 (ARF1)-GTPase, and its effector ARF-guanine-exchange factor BIGs, to the TGN (Boutté et al., 2013; Gendre et al., 2011; Jonsson et al., 2017). The *ech* mutant also displays

the abnormal TGN morphology and defects in transport of polysaccharides, including hemicelluloses and pectins, BRI1, and auxin influx carrier AUX1 to the PM (Boutté et al., 2013; Gendre et al., 2011, 2013). Since recruitment and formation of AP-1/CCV at the TGN requires ARF1 (although direct evidence is lacking in plants) (Paczkowski et al., 2015; Ren et al., 2013), ECH might be required for the generation of secretory-trafficking zone. Besides, recently identified TGNap1 is also an interesting candidate. TGNap1 was reported to bridge the GA-TGN and microtubule as well as to be required for the maintenance of structural integrity of the GA-TGN membrane and the biogenesis of the GI-TGN (Renna et al., 2018). Intriguingly, both ECH and TGNap1 interact with YIP4 proteins that are TGN-localized multispanning membrane proteins of yet largely unknown function, which are known however to play a key role in secretion of cell wall polysaccharides (Gendre et al., 2013; Renna et al., 2018). Thus, although the mechanism responsible for generating zones of the TGN remains unknown, the interplay of these proteins might be a key factor. Another possible mechanism is that lipids provide the platform to generate the zones. By biochemical approaches, Yohann Boutte and colleagues demonstrated that sphingolipids display distinct distribution throughout the TGN (Wattelet-Boyer et al., 2016). These TGN-resident lipids can probably provide the platform equivalent to well-characterized lipid rafts on the PM. Differential enrichment of sphingolipids with α-hydroxylated very long chain fatty acids (hVLCFAs) in the TGN is important for polar secretory trafficking of PIN2 and the TGN morphology (Wattelet-Boyer et al., 2016). Inhibition of enrichment of sphingolipids with hVLCFAs in the TGN induced by metazachlor (Wattelet-Boyer et al., 2016) seems to phenocopy *ap1m2* mutants, as seen in *ap1m2* mutant which exhibits irregular distribution of PIN2 (J.-G. Wang et al., 2013), suggesting sphingolipids with hVLCFAs and AP-1 function in the same secretory trafficking pathway. Comprehensive

investigation of these proteins and lipids will provide further insights into the zone biogenesis in the TGN.

Chapter 5: Conclusion and Perspective

The TGN is conceptually believed to function as the platform for different trafficking pathways (Griffiths & Simons, 1986; Y. Ito & Boutté, 2020). Such hypothesis has been mainly postulated by independent studies focusing on the single trafficking pathway, such as secretory trafficking or vacuolar/lysosomal trafficking. However, little has been known about how the TGN provides venues for sorting of cargo proteins with different destinies. In the present study, I demonstrated clearly that the single TGN has two distinct zones for secretory and vacuolar trafficking routes by the state-of-the-art visualization technique. Secretory cargo VAMP721, cargo adaptor AP-1, and clathrin exclusively localize to the zone involved in secretory trafficking, whereas vacuolar cargo VAMP727 and cargo adaptor AP-4 localize another zone involved in vacuolar trafficking on the same TGN. Taking advantage of the live-imaging by SCLIM, I also discovered that AP-1 and AP-4, which play roles in the formation of transport vesicles, exhibited different dynamics. The former AP-1 leaves the GA-TGN with clathrin in the form of a cluster while the latter AP-4 seem to persist on the GA-TGN. This unexpected phenomenon might suggest that these trafficking pathways are regulated in distinct fashions. Although molecular contributors to the vacuolar-trafficking pathway mediated by plant AP-4 have been well characterized among eukaryotes (equivalent to the mannose 6-phosphate pathway in mammal and the CPY pathway in yeast) (Cui et al., 2016; Minamino & Ueda, 2019), the fashion of cargo transporting from the TGN into this pathway has never been observed in living cells, mostly because of technical problems. Recently, pulse-chase-type experimental systems for the biosynthetic cargo protein transport, such as a retention using selective hooks (RUSH) system in mammalian cultured cells (Boncompain et al., 2012) and a temperature-controlled system in budding yeast (Kurokawa et al., 2014), have been proposed and successfully applied in other organisms.

Unfortunately, such systems have not been established in plant cells yet. The state-of-the-art visualization technique in combination with these pulse-chase methods will be established soon in plant cells as a powerful tool for investigating the vacuolar-trafficking pathway as well as the secretory-trafficking pathway. Such a system would also shed light on still unanswered questions; how and when are cargo proteins are segregated? I strongly believe that the discoveries made in this study provide a foundation for future studies aiming to dissect the role of the TGN.

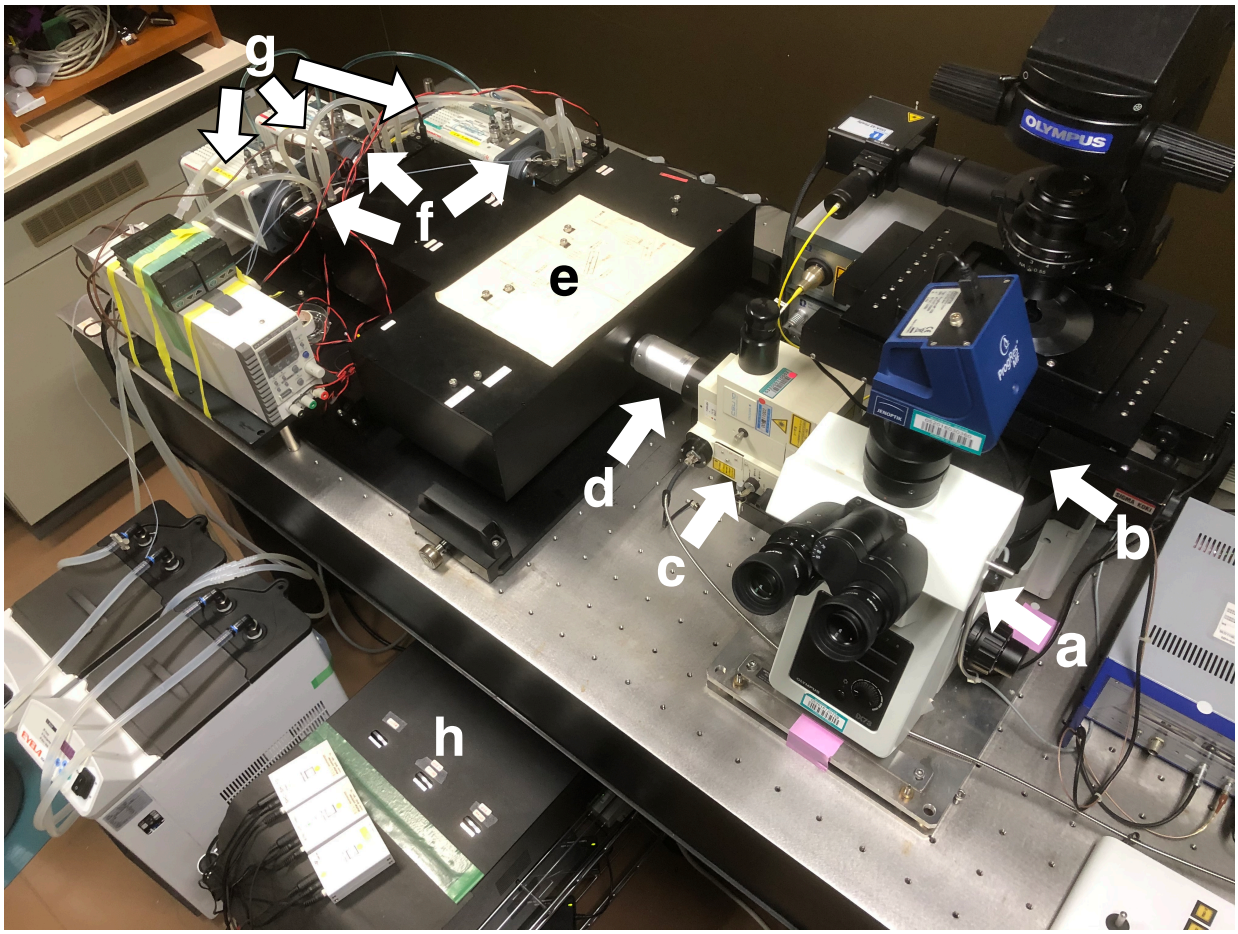

Figure 1. Overview of SCLIM setup.
The inverted microscope (a) is equipped with an ultra-fast piezo actuator (b), a custom-made spinning-disk confocal scanner (c), 4× intermediate lens (d), a custom-made spectroscopic unit (e), 3 image intensifiers with a custom-made cooling system (f), 3 EM-CCD cameras (g), and 3 excitation lasers (h).

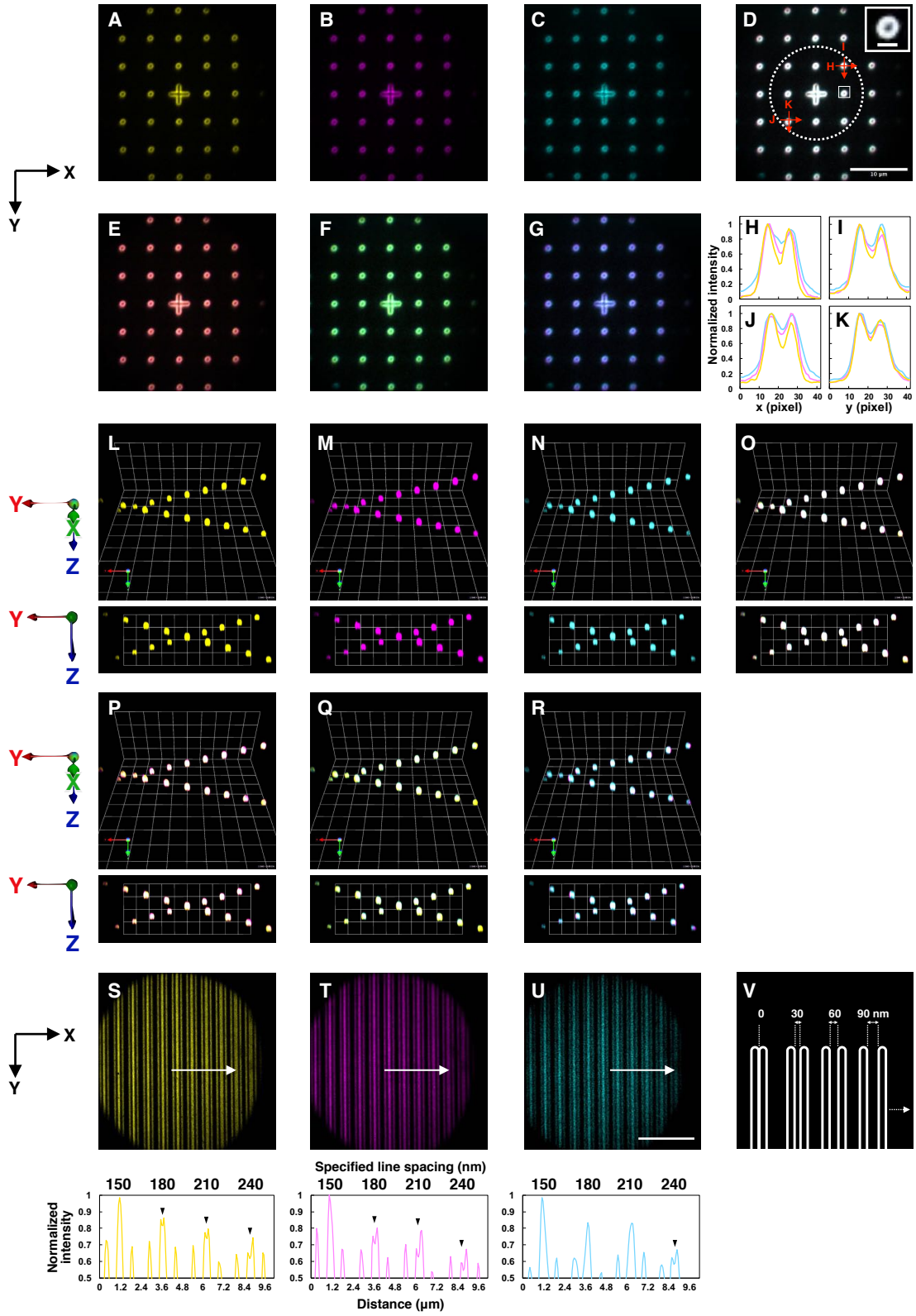

Figure 2. Three different patterns in the ARGO-SIM slide were observed by SCLIM.
(A–K) Representative confocal plane images of "matrix of rings" in the ARGO-SIM slide for 3 different channels (Green, **A**; Red, **B**; and Infrared, **C**), and the superposition of these channels **(D–G)**. The inset in **D** shows the magnification image of the ring in the boxed area. The dotted circle in **D** represents the observation area in the present study. **(H–K)** The intensity profiles for 2 rings at the upper right and under left in the observation area. It should be noted that lateral shift between the 3 channels is less than 1 pixel.
(L–R) "Crossing stair type of rings" with 2 μm steps was observed to evaluate the shift in Z-axis and the accuracy of 3D reconstruction. Green, **(L)**, Red **(M)**, Infrared **(N)**, and the superposition of these channels **(O–R)**.
(S–U) "Nanoscale ruler" with gradually increased spacing in steps of 30 nm from left to right was observed to assess the lateral resolution in the green, red, and infrared part of the fluorescent spectra. Graphs show the intensity profiles along arrows with a line width of 5 pixels. The specified line space of 180 nm, 180 nm, and 240 nm are resolved in green **(S)**, red **(T)**, and infrared **(U)** channels, respectively (arrowheads). **(V)** The schematic image of the nanoscale ruler. Scale bars = 10 μm (**D** and **U**); 1 μm (inset in **D**); Grid width = 3.08 μm **(L–R)**.

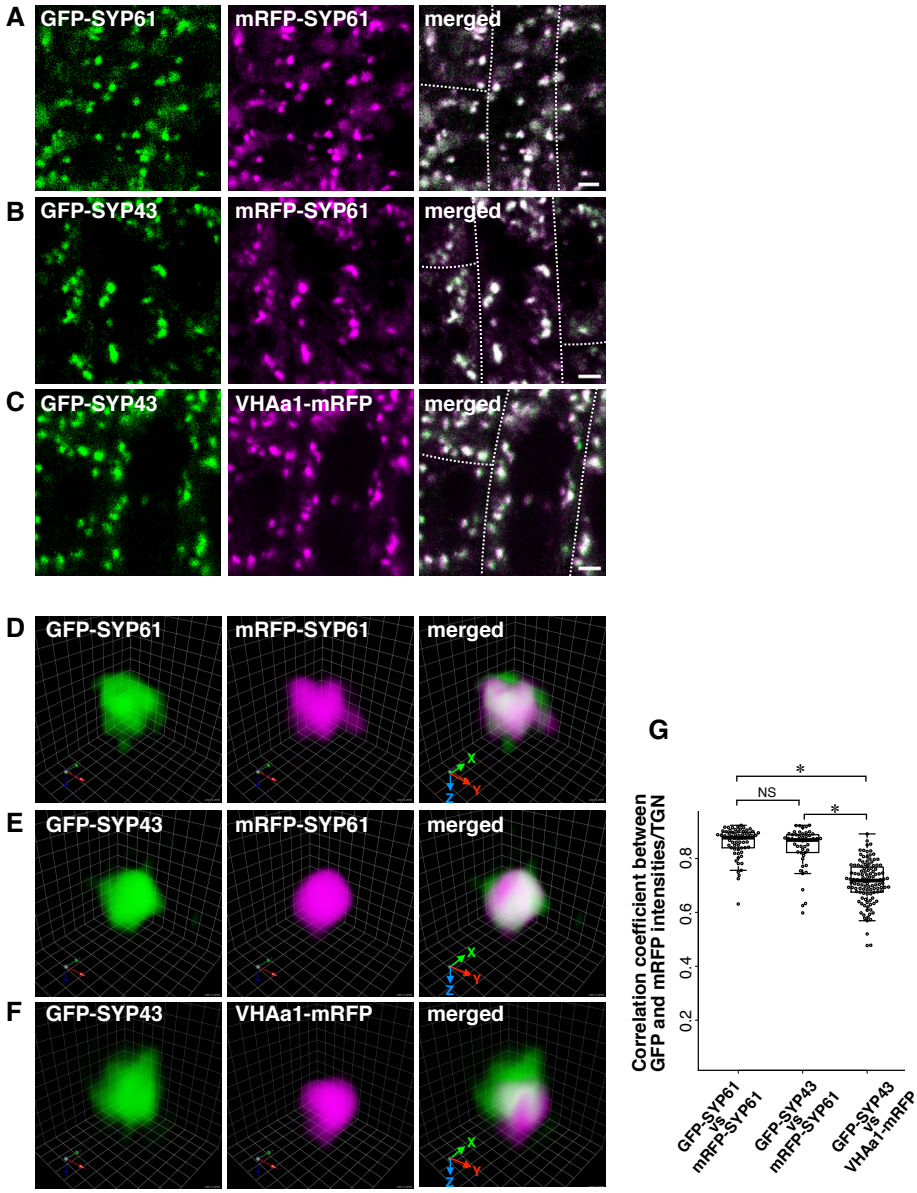

Figure 3. Differential distribution of TGN-markers.
(A–F) Confocal images under conventional CLSM **(A–C)** or 3D images under SCLIM **(D–F)** of GFP-SYP61 × mRFP-SYP61 **(A, D)**, GFP-SYP43 × mRFP-SYP61 **(B, E)**, or GFP-SYP43 × VHAa1-mRFP **(C, F)** in the epidermal cells of the root elongation zone.
Scale bars = 5 μm **(A–C)**. Grid width = 0.234 μm **(D–F)**. Dashed lines indicate cell edges.
(G) 3D colocalization analysis of the TGN markers: n = 64, 50, and 118 TGNs for GFP-SYP61 vs mRFP-SYP61, GFP-SYP43 vs mRFP-SYP61, and GFP-SYP43 vs VHAa1-mRFP, respectively, from 5 or more biological replicates.
Two-sided Steel-Dwass test;
$P = 0.86$ (Left: GFP-SYP61 × mRFP-SYP61 vs GFP-SYP43 × mRFP-SYP61),
$P = 3.0 \times 10^{-14}$ (Top: GFP-SYP61 × mRFP-YP61 vs GFP-SYP43 × VHAa1-mRFP),
$P = 2.2 \times 10^{-7}$ (Right: GFP-SYP43 × mRFP-SYP61 vs GFP-SYP43 × VHAa1-mRFP);
*$P < 0.01$, NS = nonsignificant.
Boxes represent 25% and 75% quartiles, lines within the box represent the median, and whiskers represent the minimum and maximum values within 1.5x the interquartile range.

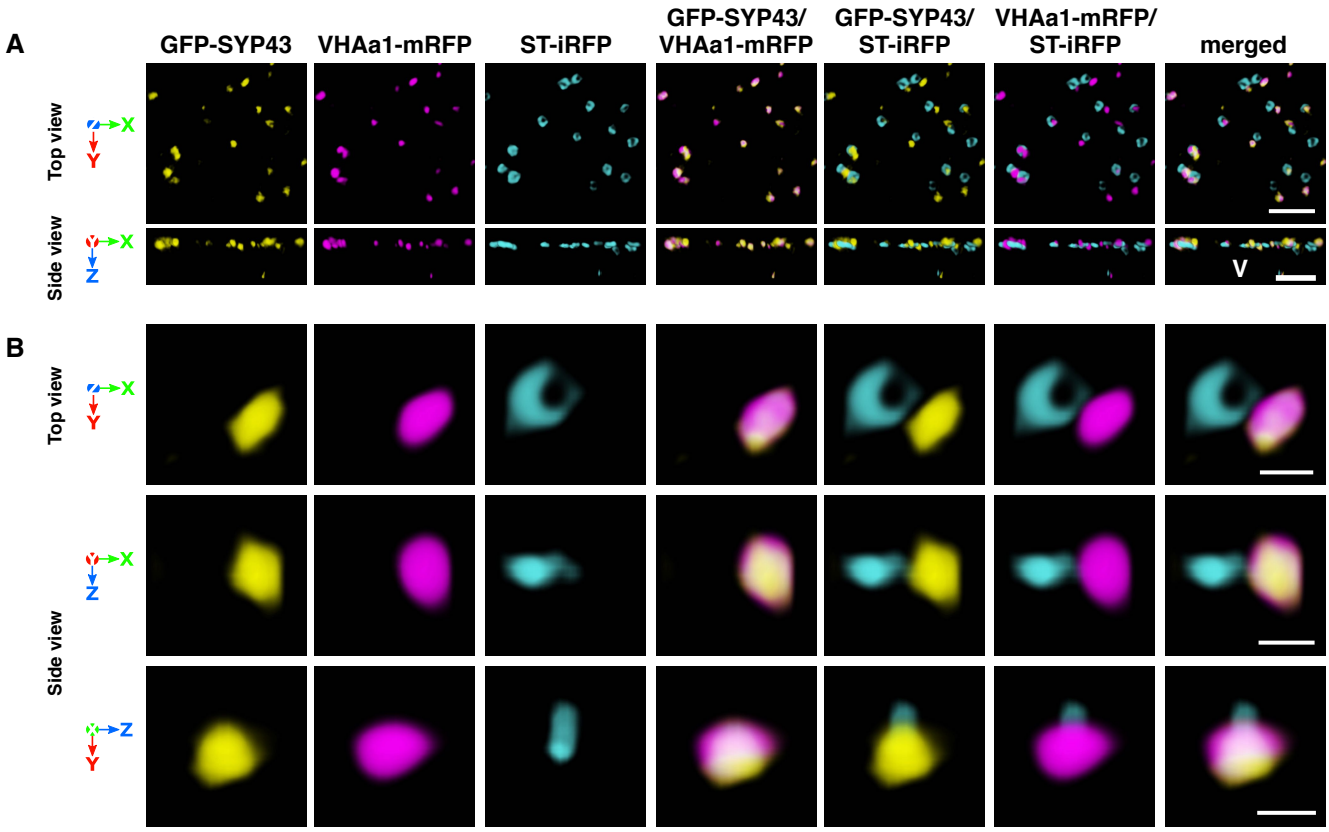

Figure 4. Triple-color imaging of the Golgi-marker and two TGN-markers.
(A and B) 3-color SCLIM imaging of root epidermal cells in the elongation zone of Arabidopsis expressing GFP-SYP43 × VHAa1-mRFP × ST-iRFP. **(B)** Multi-angle magnified 3D images of the boxed area in **A**.
V, vacuole area. Scale bars = 5 μm **(A)**; 1 μm **(B)**.

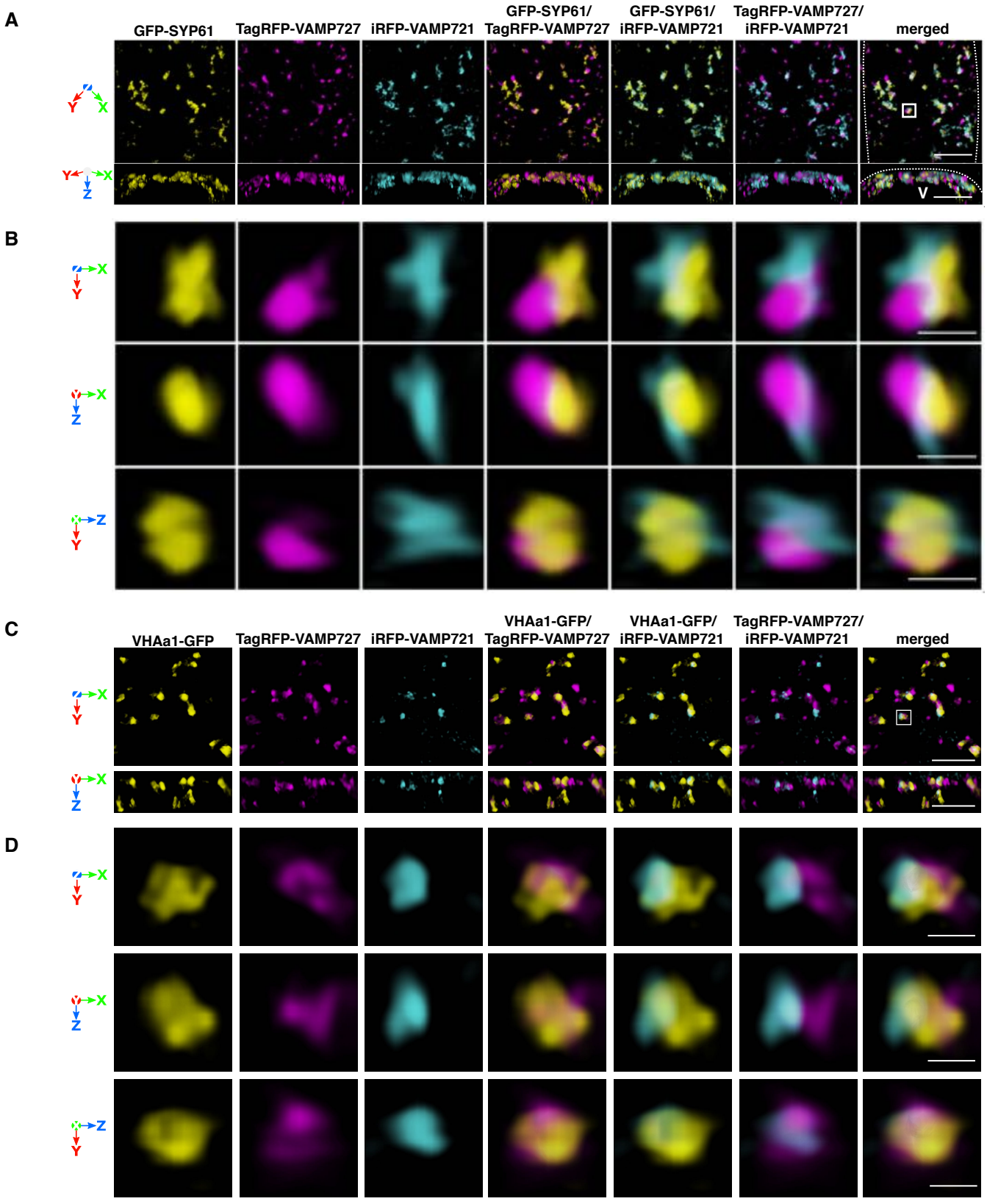

Figure 5. Differential distribution of TGN-localized cargo proteins.
(A–D) 3D images of Arabidopsis expressing TagRFP-VAMP727 and iRFP-VAMP721 with TGN-markers, GFP-SYP61 **(A, B)** or VHAa1-GFP **(C, D)**, in the epidermal cell of the root elongation zone under SCLIM.
(B and D) Multi-angle magnified 3D images of the boxed area in **A** and **C**, respectively.
Scale bars = 5 μm **(A, C)**; 1 μm **(B, D)**. Dashed lines indicate cell edges. V, vacuole area.

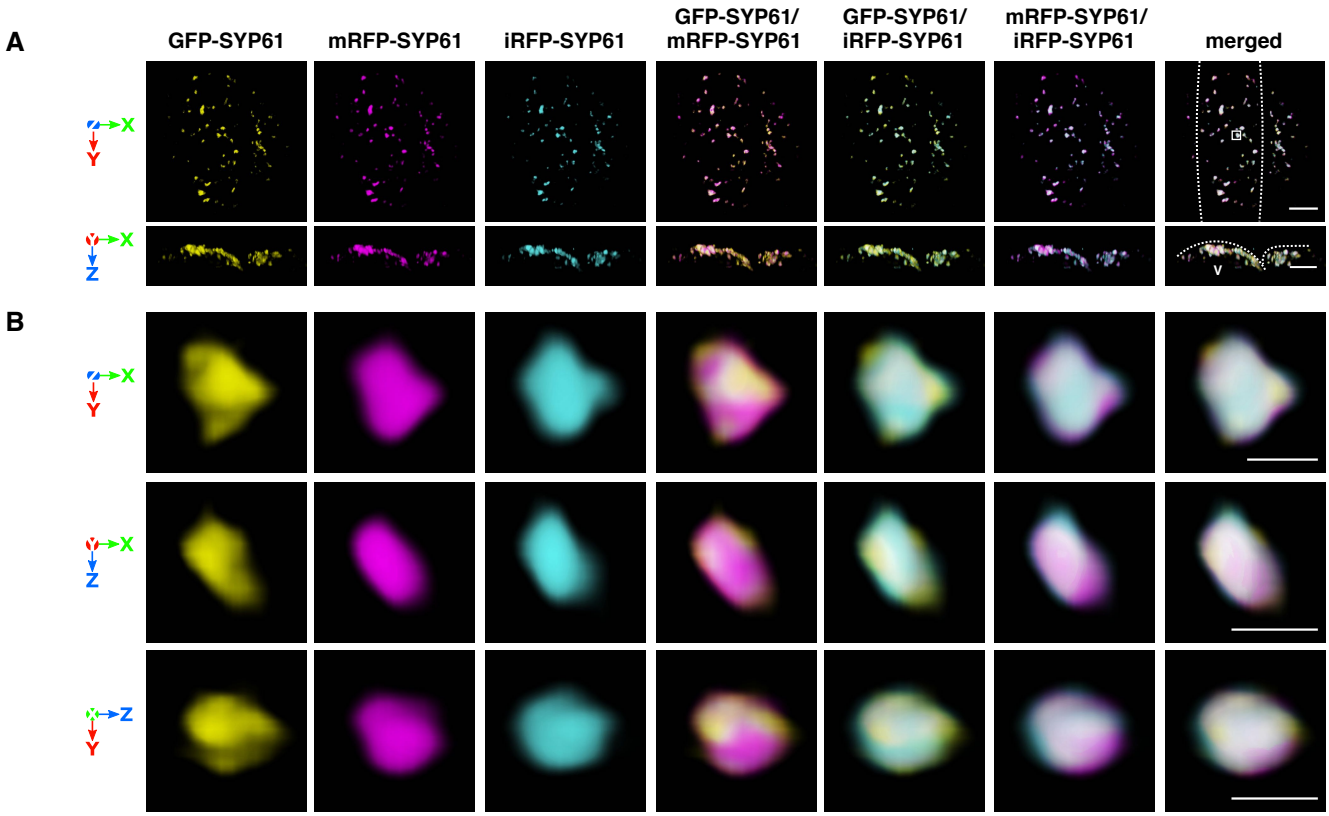

Figure 6. Different fluorescent proteins-tagged TGN-markers as the control.
(A and B) 3-color SCLIM imaging of root epidermal cells in the elongation zone of Arabidopsis expressing GFP-SYP61 × mRFP-SYP61× iRFP-SYP61. **(B)** Multi-angle magnified 3D images of the boxed area in **A**.
Dashed lines indicate cell edges. V, vacuole area. Scale bars = 5 μm **(A)**; 1 μm **(B)**.

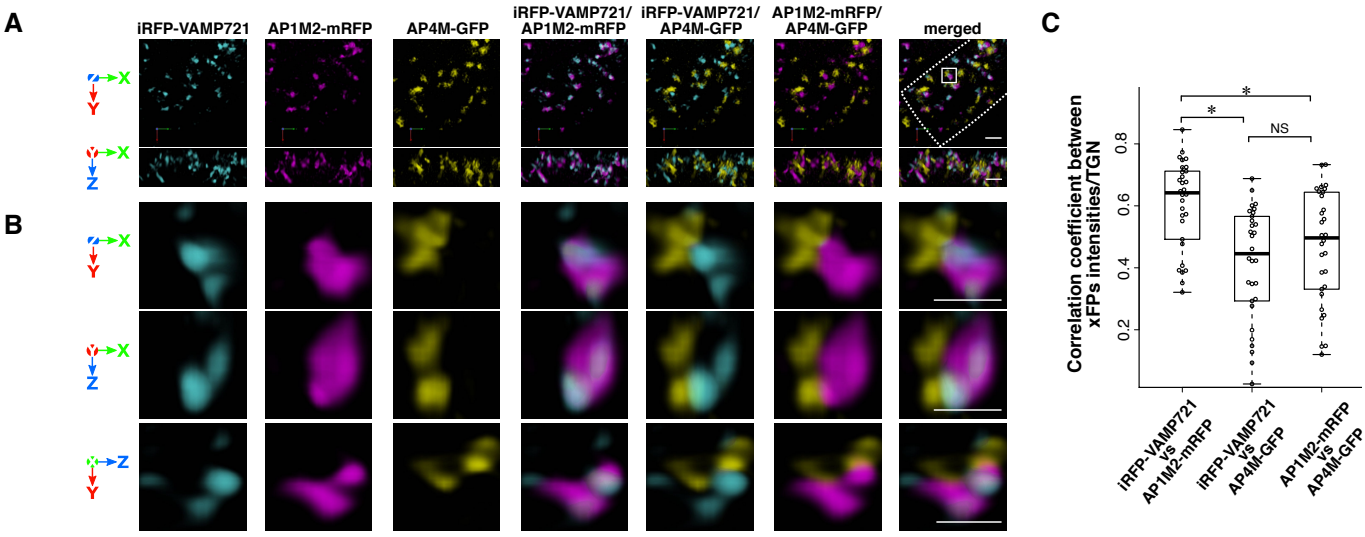

Figure 7. AP-1, but not AP-4, colocalize with VAMP721.
(A and B) 3-color SCLIM imaging of root epidermal cells in the elongation zone of Arabidopsis expressing iRFP-VAMP721 × AP1M2-mRFP × AP4M-GFP
(B) Multi-angle magnified 3D images of the boxed area in **A**. Scale bars = 2 μm **(A)**; 1 μm **(B)**. Dashed lines indicate cell edges.
(C) 3D colocalization analysis between μ-subunits of APs and VAMP721 on the TGN: n = 30 TGNs for each experiment, from 3 biological replicates.
Two-sided Steel-Dwass test;
$P = 1.8 \times 10^{-4}$ (Left: iRFP-VAMP721 × AP1M2-mRFP versus iRFP-VAMP721 × AP4M-GFP),
$P = 8.3 \times 10^{-3}$ (Top: iRFP-VAMP721 × AP1M2-mRFP versus AP1M2-mRFP × AP4M-GFP),
$P = 0.51$ (Right: iRFP-VAMP721 × AP4M-GFP versus AP1M2-mRFP × AP4M-GFP);
*$P < 0.01$, NS = nonsignificant. Boxes represent 25% and 75% quartiles, lines within the box represent the median, and whiskers represent the minimum and maximum values within 1.5x the interquartile range.

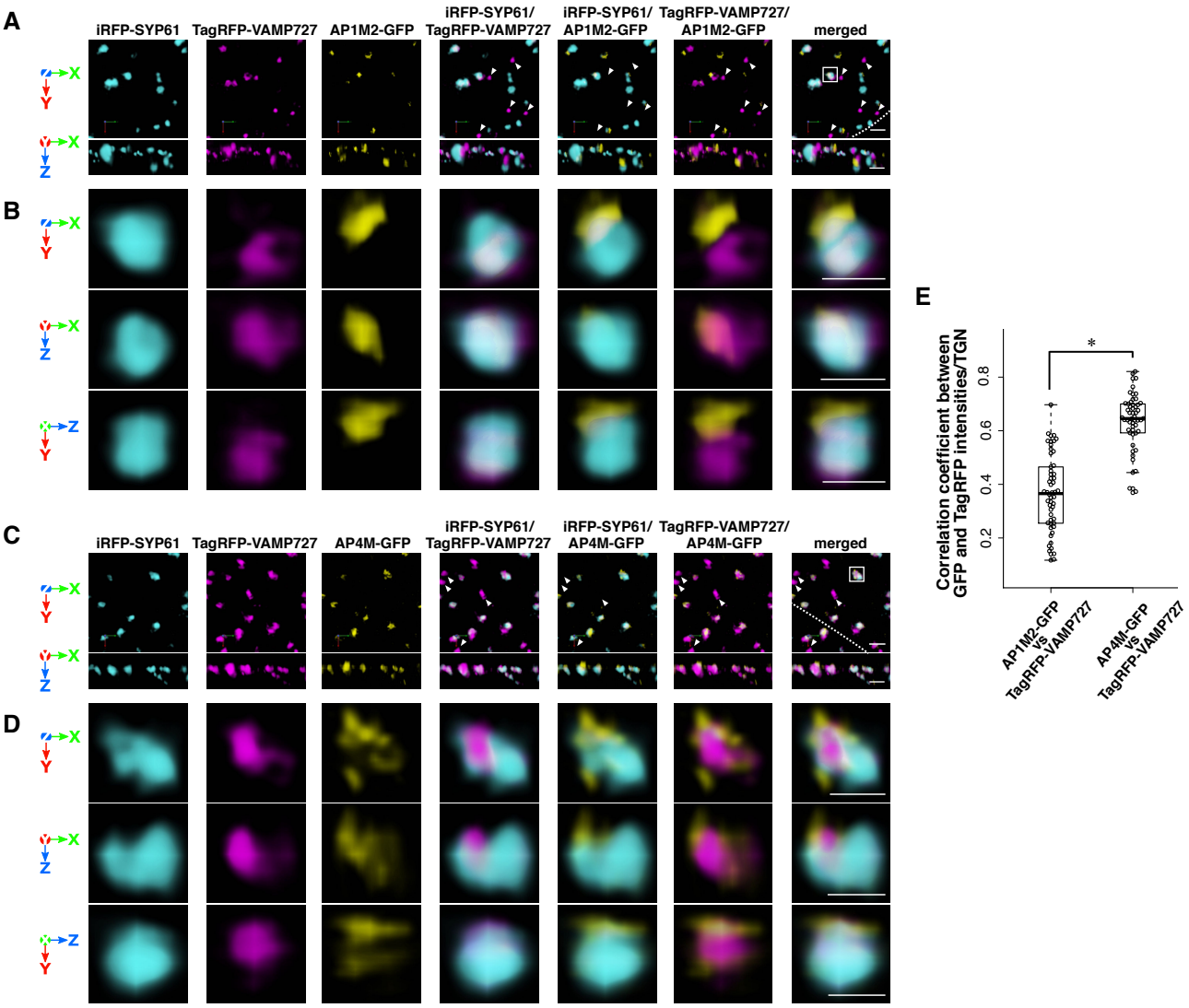

Figure 8. AP-4, but not AP-1, colocalize with VAMP727.
(A–D) 3-color SCLIM imaging of root epidermal cells in the elongation zone of Arabidopsis expressing iRFP-SYP61 × TagRFP-VAMP727 × AP1M2-GFP **(A, B)**, or iRFP-SYP61 × TagRFP-VAMP727 × AP4M-GFP **(C, D)**. **(B and D)** Multi-angle magnified 3D images of the boxed area in **A** and **C**, respectively. Scale bars = 2 μm **(A, C)**; 1 μm **(B, D)**. Arrowheads indicate TagRFP-VAMP727 without iRFP-SYP61 and APs-GFP signals. Dashed lines indicate cell edges.
(E) 3D colocalization analysis between μ-subunits of APs and VAMP727 on the TGN: n = 54 TGNs for each experiment, from 5 biological replicates. Two-sided Wilcoxon rank-sum test; $P = 1.5 \times 10^{-14}$; $*P < 0.01$.
Boxes represent 25% and 75% quartiles, lines within the box represent the median, and whiskers represent the minimum and maximum values within 1.5x the interquartile range.

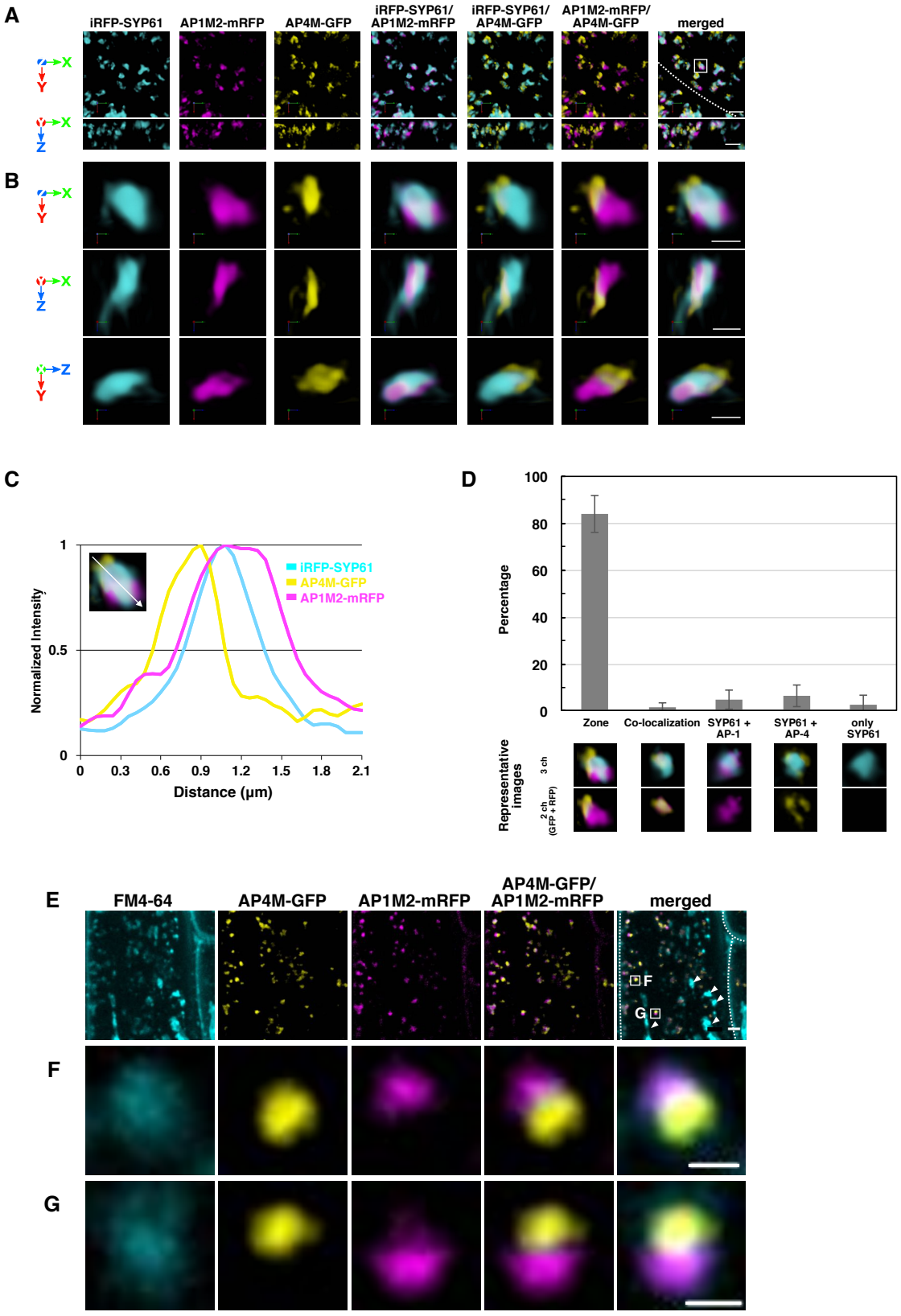

Figure 9. Distinct suborganellar localization of AP-1 and AP-4 in the TGN.
(A and B) 3-color SCLIM imaging of root epidermal cells in the elongation zone of Arabidopsis expressing iRFP-SYP61 × AP1M2-mRFP × AP4M-GFP. **(B)** Multi-angle magnified 3D images of the boxed area in **A**.
(C) A graph shows normalized fluorescence intensity profile across a TGN of boxed area in **A**. **(D)** A graph represents the percentage of TGNs in which AP-1 and AP-4 localized on distinct zone, or colocalize, or either of them is present, or neither. A cell was picked from a SCLIM 3D image, and round- or ellipsoid-like signals from the TGN-marker were counted. In total 7 independent cells (30–65 TGNs) were analyzed. Error bars = SD.
(E–G) Confocal images of FM4-64 × AP4M-GFP × AP1M2-mRFP under conventional CLSM with a high-resolution objective lens after 6 min of FM4-64 uptake. **(E)** Low-magnification images. **(F and G)** High-magnification images of the boxed area in **E**. Dashed lines indicate cell edges. Arrowheads show strong fluorescence signals of FM4-64 from the plasma membrane/cell wall.
Scale bars = 2 μm **(A, E)**; 1 μm **(B, F, G)**. Dashed lines indicate cell edges.

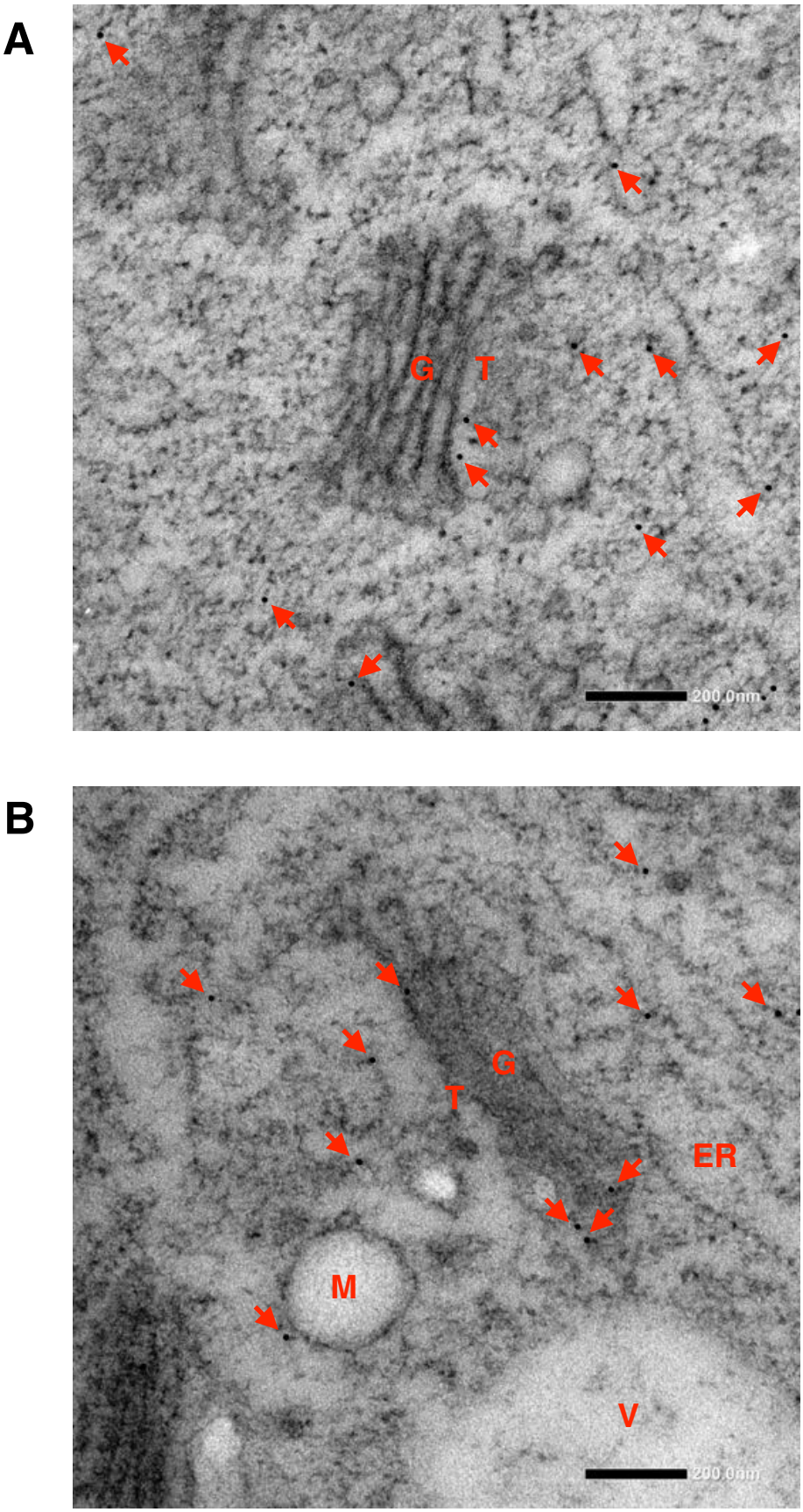

Figure 10. Representative immunogold labeling of AP1M2-GFP or AP4M-GFP with an anti-GFP antibody. **(A and B)** Arabidopsis root cells expressing either AP1M2-GFP **(A)** or AP4M-GFP **(B)** were fixed by high-pressure freezing/freeze substitution with anhydrous acetone containing 0.25% glutaraldehyde and 0.1% uranyl acetate, and ultrathin sections were prepared. The ultrathin sections were stained with anti-GFP antibodies (mix of Invitrogen A11122 and Abcam ab290). Arrows show gold particles. ER, Endoplasmic reticulum; G, Golgi; T, GA-TGN; M, Multivesicular endosome; V, vacuole. Scale bars = 200 nm.

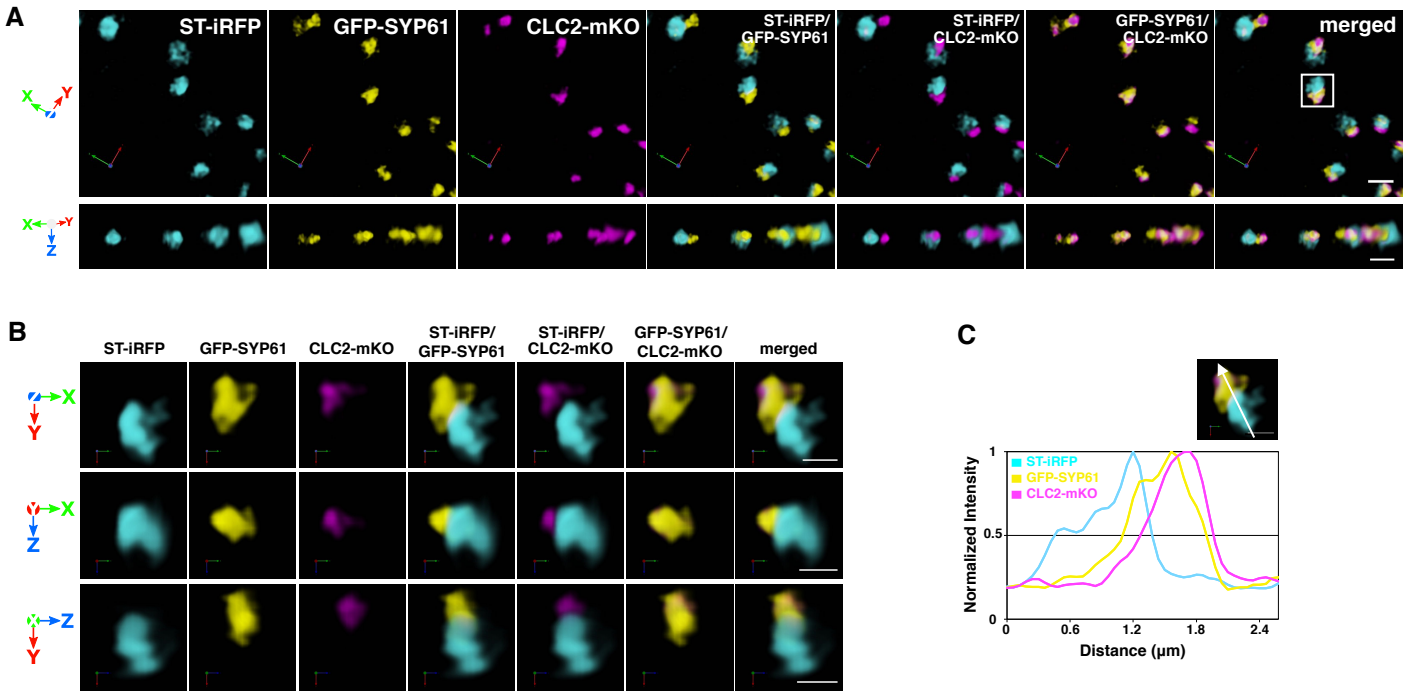

Figure 11. Clathrin localizes on the *trans*-side membrane of the TGN.
(A and B) 3D images of ST-iRFP (*trans*-Golgi apparatus), GFP-SYP61 (TGN), and CLC2-mKO (clathrin) in the epidermal cell of the root elongation zone under SCLIM. **(B)** Multi-angle magnified images of boxed area in **A**. **(C)** A graphs show normalized fluorescence intensity profile across a Golgi apparatus to clathrin of boxed area in **A**.

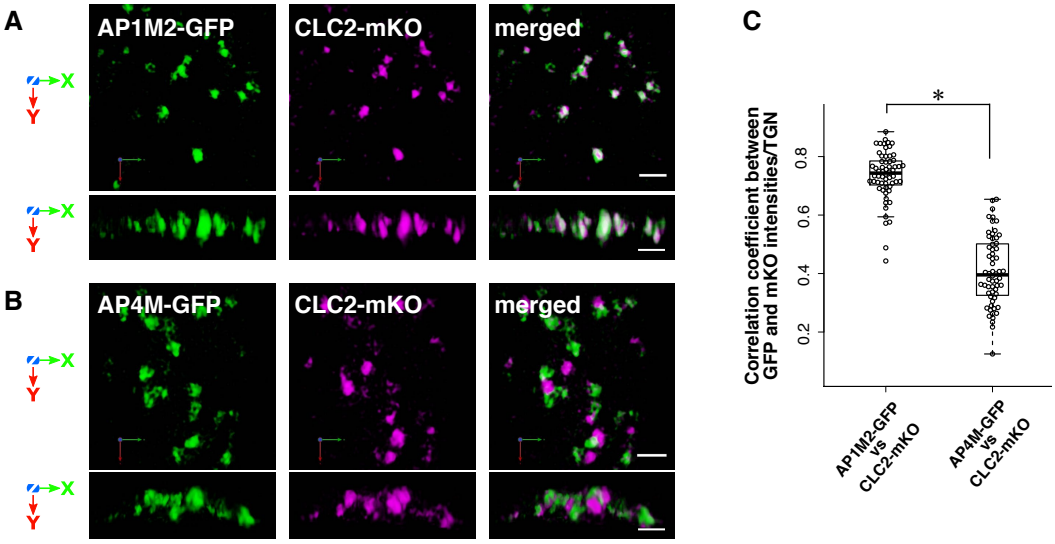

Figure 12. Clathrin localizes on the *trans*-side membrane of the TGN.
(A and B) 3D images of AP1M2-GFP and CLC2-mKO **(A)** or AP4M-GFP and CLC2-mKO **(B)** in the epidermal cells of the root elongation zone under SCLIM. Upper panels: top view; lower panels: side view. Scale bars = 2 μm **(A)**; 1 μm **(B)**.
(C) 3D colocalization analysis between μ-subunits of APs and CLC2: n = 60 TGNs for each experiment, from 5 biological replicates. Two-sided Wilcoxon rank-sum test; $P = 2.2 \times 10^{-16}$; $*P < 0.01$.
Boxes represent 25% and 75% quartiles, lines within the box represent the median and whiskers represent the minimum and maximum values within 1.5x the interquartile range.

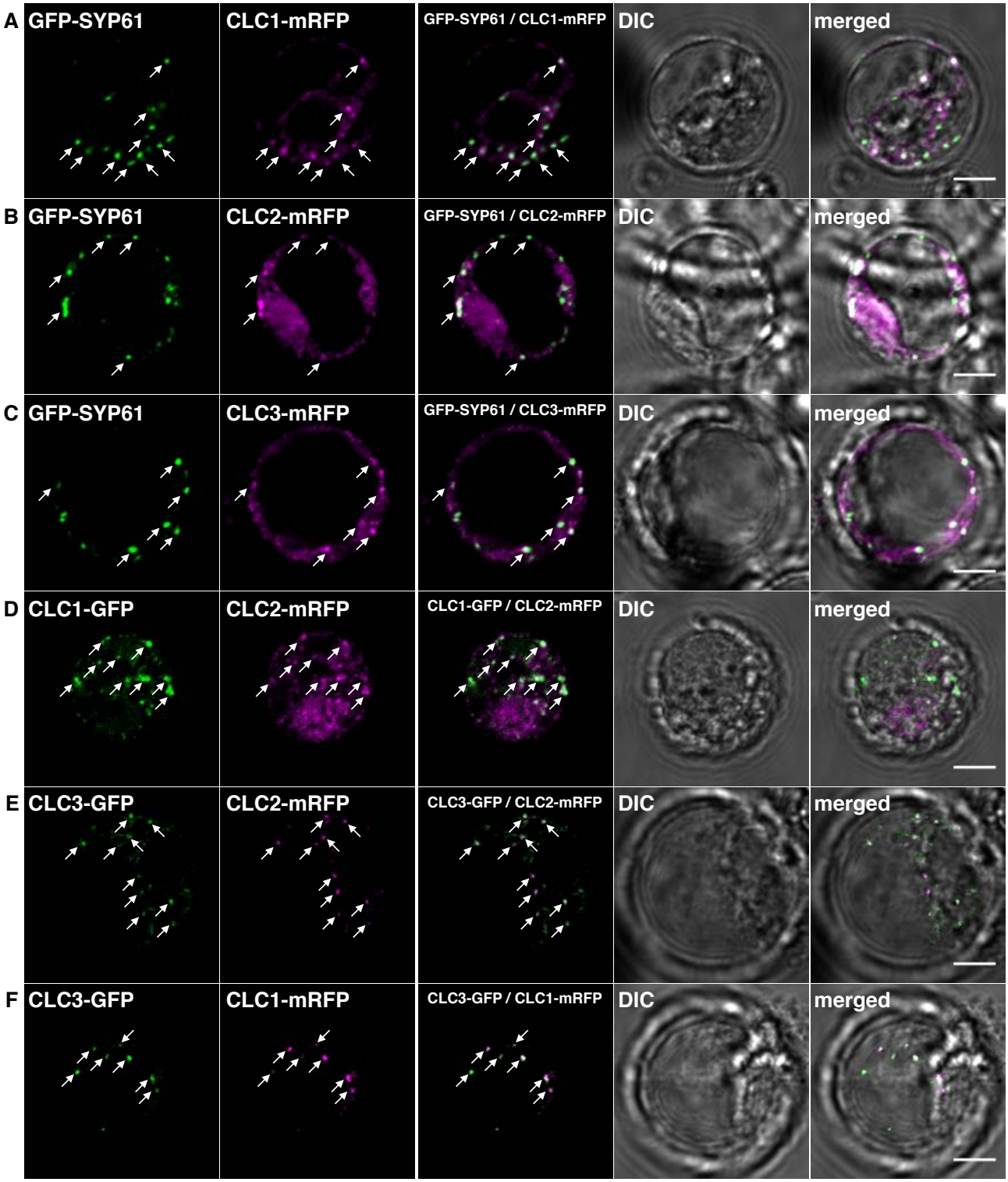

Figure 13. Subcellular localization of fluorescent protein-tagged CLCs.
(A–F) Confocal images of GFP-SYP61 and CLC1-mRFP **(A)**, GFP-SYP61 and CLC2-mRFP **(B)**, GFP-SYP61 and CLC3-mRFP **(C)**, CLC1-GFP and CLC2-mRFP **(D)**, CLC3-GFP and CLC2-mRFP **(E)**, or CLC3-GFP and CLC1-mRFP **(F)** transiently expressed in the protoplasts of Arabidopsis suspension cultured cells. Arrows indicate colocalized signals in endomembranes. DIC, differential interference contrast micrograph. Scale bars = 5 μm.

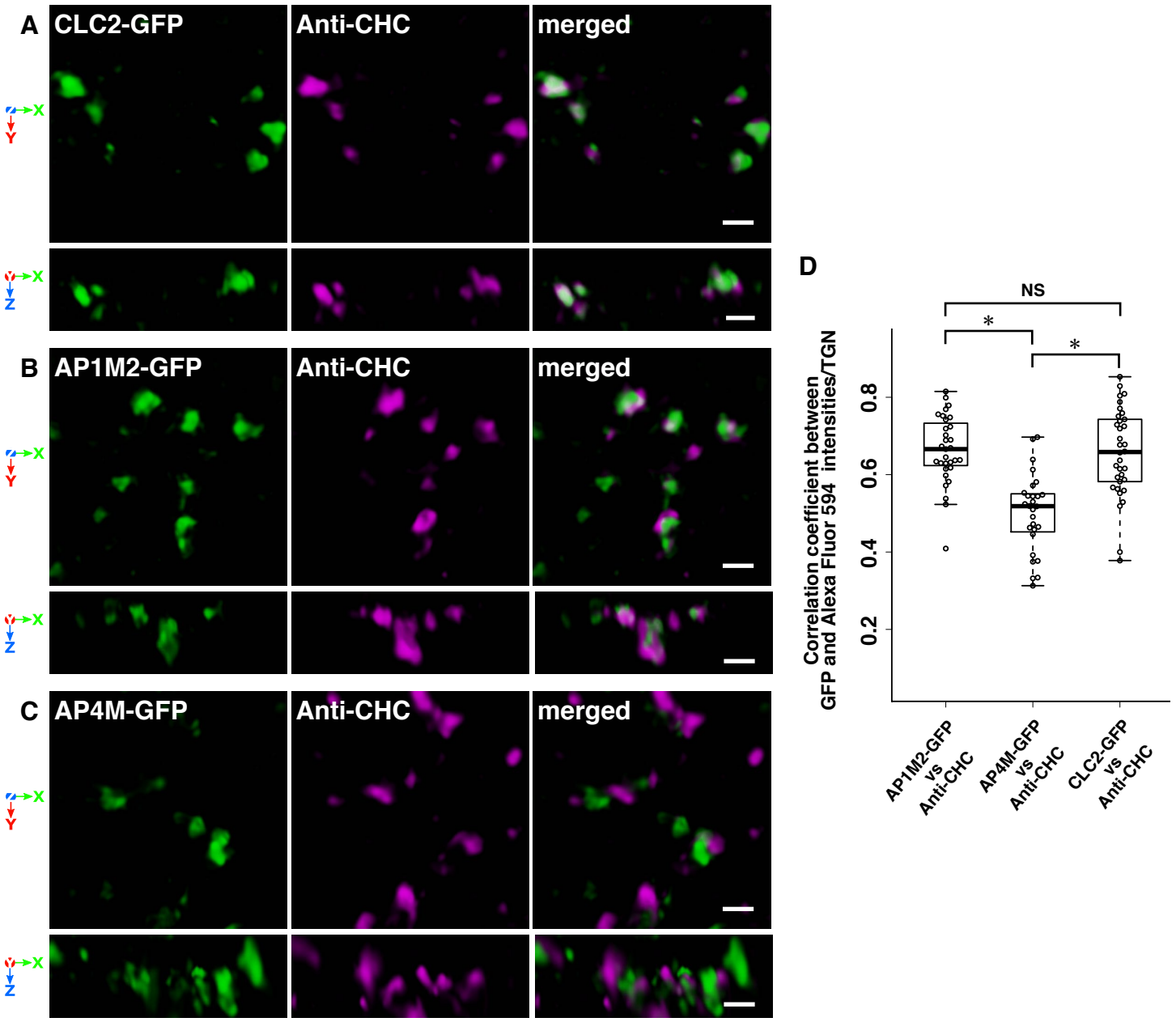

Figure 14. Subcellular localization of endogenous CHCs.
(A–C) 3D images of CLC2-GFP **(A)**, AP1M2-GFP **(B)**, and AP4M-GFP **(C)** with anti-CHCs (Alexa 594) in the epidermal cells of the root elongation zone under SCLIM.
(D) 3D colocalization analysis: $n = 31$, 28, and 34 TGNs for AP1M2-GFP vs Anti-CHC, AP4M-GFP vs Anti-CHC, and CLC2-GFP vs Anti-CHC, respectively, from 3 biological replicates.
Two-sided Steel-Dwass test;
$P = 8.3 \times 10^{-7}$ (Left: AP1M2-GFP × Anti-CHC versus AP4M-GFP × Anti-CHC),
$P = 0.9$ (Top: AP1M2-GFP × Anti-CHC versus CLC2-GFP × Anti-CHC),
$P = 3.5 \times 10^{-6}$ (Right: AP4M-GFP × Anti-CHC versus CLC2-GFP × Anti-CHC);
*$P < 0.01$, NS = nonsignificant. Boxes represent 25% and 75% quartiles, lines within the box represent the median, and whiskers represent the minimum and maximum values within 1.5x the interquartile range. Scale bars = 1 μm.

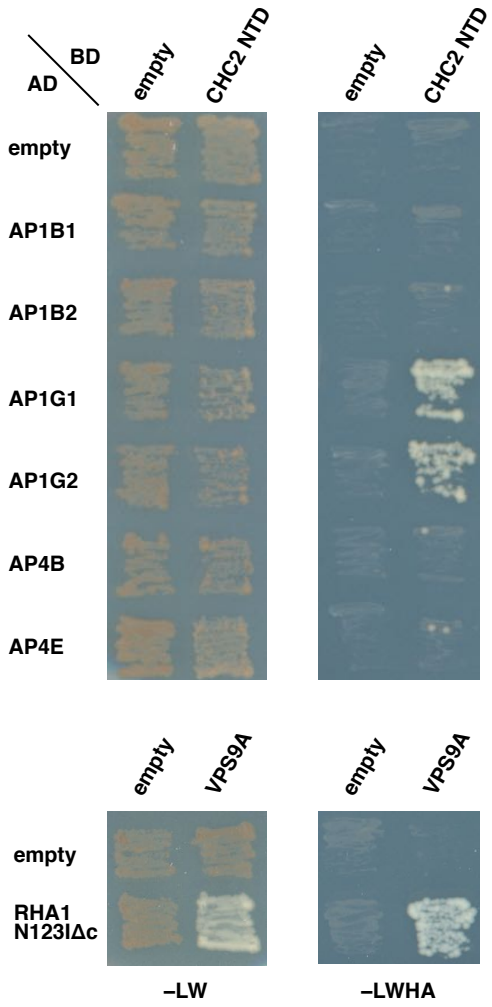

Figure 15. AP-1 interacts with Clathrin in the yeast two-hybrid experiment.
Yeast two-hybrid interaction assay between AP-1 or AP-4 vs clathrin. Large subunits of AP-1 and AP-4 were expressed as a fusion protein with an activation domain (AD) and an amino-terminal domain of CHC2 (CHC2 NTD) was expressed as a fusion protein with a DNA binding domain (BD) in the yeast strain AH109. Transformants were plated on medium without Leu, Trp, His, and adenine (-LWHA) to test for interactions between two proteins or on medium without Leu and Trp (-LW) for 4 d at 30˚C. The assay for RHA1 N123IΔc vs VPS9A was performed as a control experiment.

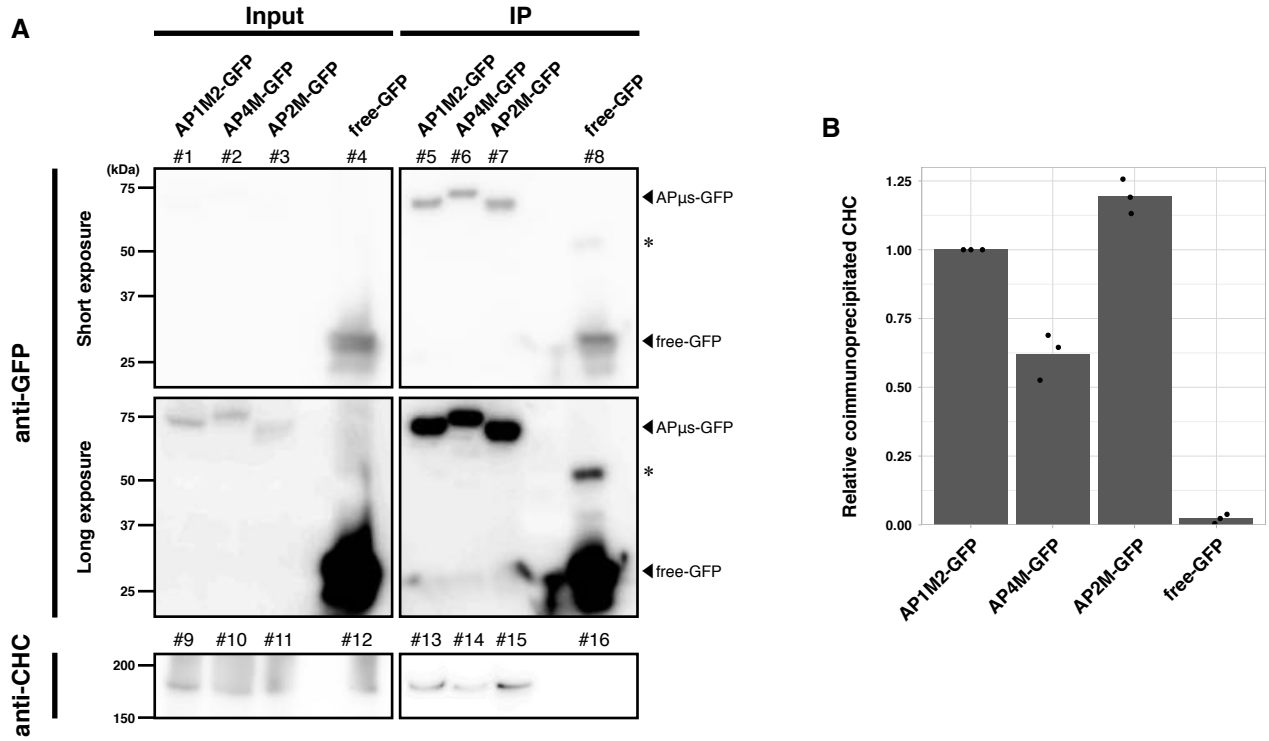

Figure 16. Co-immunoprecipitation analysis between AP complexes and clathrin.
(A) Co-immunoprecipitation analysis of immunoprecipitates with an anti-GFP antibody from seedlings expressing either AP1M2-GFP (lane #1, 5, 9, 13), AP4M-GFP (lane #2, 6, 10, 14), AP2M-GFP (positive control; lane #3, 7, 11, 15), or free-GFP (negative control; lane #4, 8, 12, 16). The immunoprecipitates were immunoblotted using anti-GFP (lane #1–8) or anti-CHC antibodies (lane #9–16). Asterisks indicate non-specific bands. Input = 16% (anti-GFP; lane #1–4); 1% (anti-CHC; lane #9–12).
(B) Densitometric quantification of CHC co-immunoprecipitated with GFP-tags. n = 3 independent experiments.

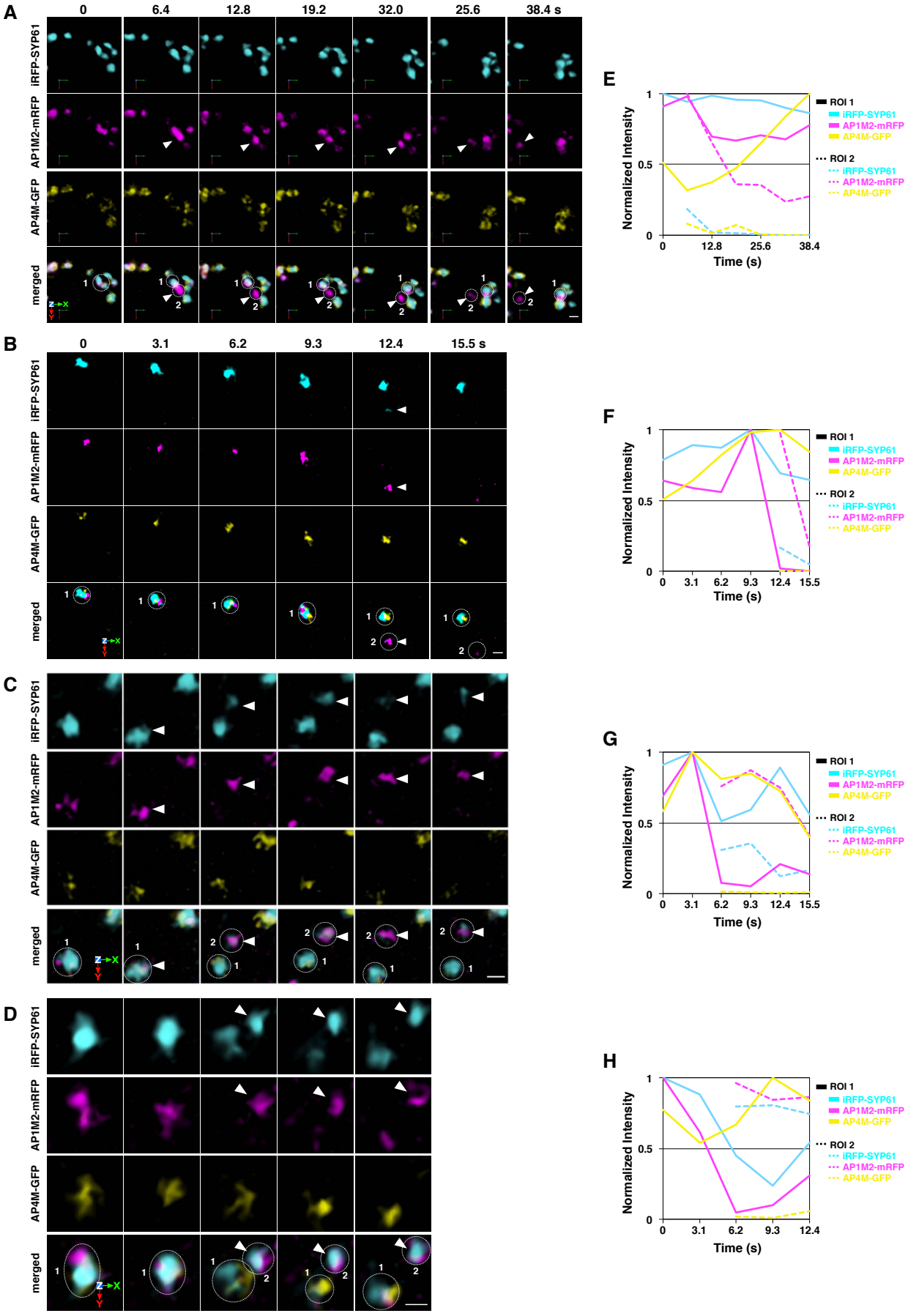

Figure 17. AP-1, but not AP-4, bud from the TGN.
(A–D) 3D time-lapse (4D) images of iRFP-SYP61, AP1M2-mRFP, and AP4M-GFP in the epidermal cells of the root elongation zone under SCLIM. Arrowheads indicate the dissociation of AP1M2-mRFP and iRFP-SYP61 from a large population of TGN labeled with iRFP-SYP61. Images are lined up every 6.4 s **(A)** or 3.1 s **(B–D)** from left to right. Scale bars = 1 μm. **(E–H)** Time course changes in relative fluorescence intensities of iRFP-SYP61, AP1M2-mRFP, and AP4M-GFP in ROIs of **A–D**.

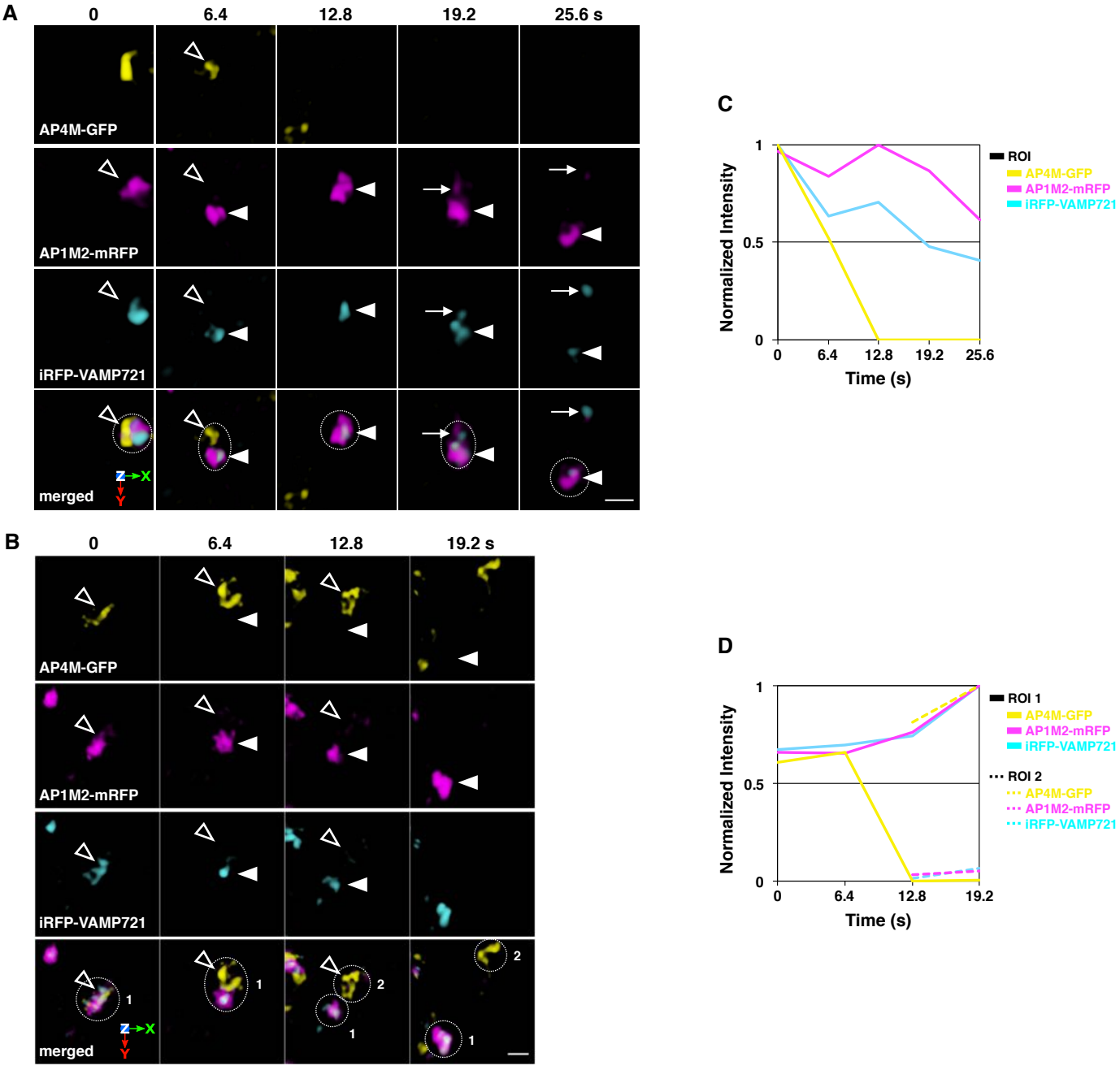

Figure 18. AP-1, but not AP-4, behaves together with VAMP721.
(A and B) 4D images of iRFP-VAMP721, AP1M2-mRFP, and AP4M-GFP in the epidermal cells of the root elongation zone under SCLIM. Arrowheads indicate AP1M2-mRFP and iRFP-VAMP721 dissociation from AP4M-GFP or the TGN (open arrowheads). A small punctum containing AP1M2-mRFP and iRFP-VAMP721 (arrows) separated from the TGN-detached structure (arrowheads). Images are lined up every 6.4 s from left to right. Scale bars = 1 μm.
(C and D) Time course changes in relative fluorescence intensities in ROIs of **A** and **B,** respectively.

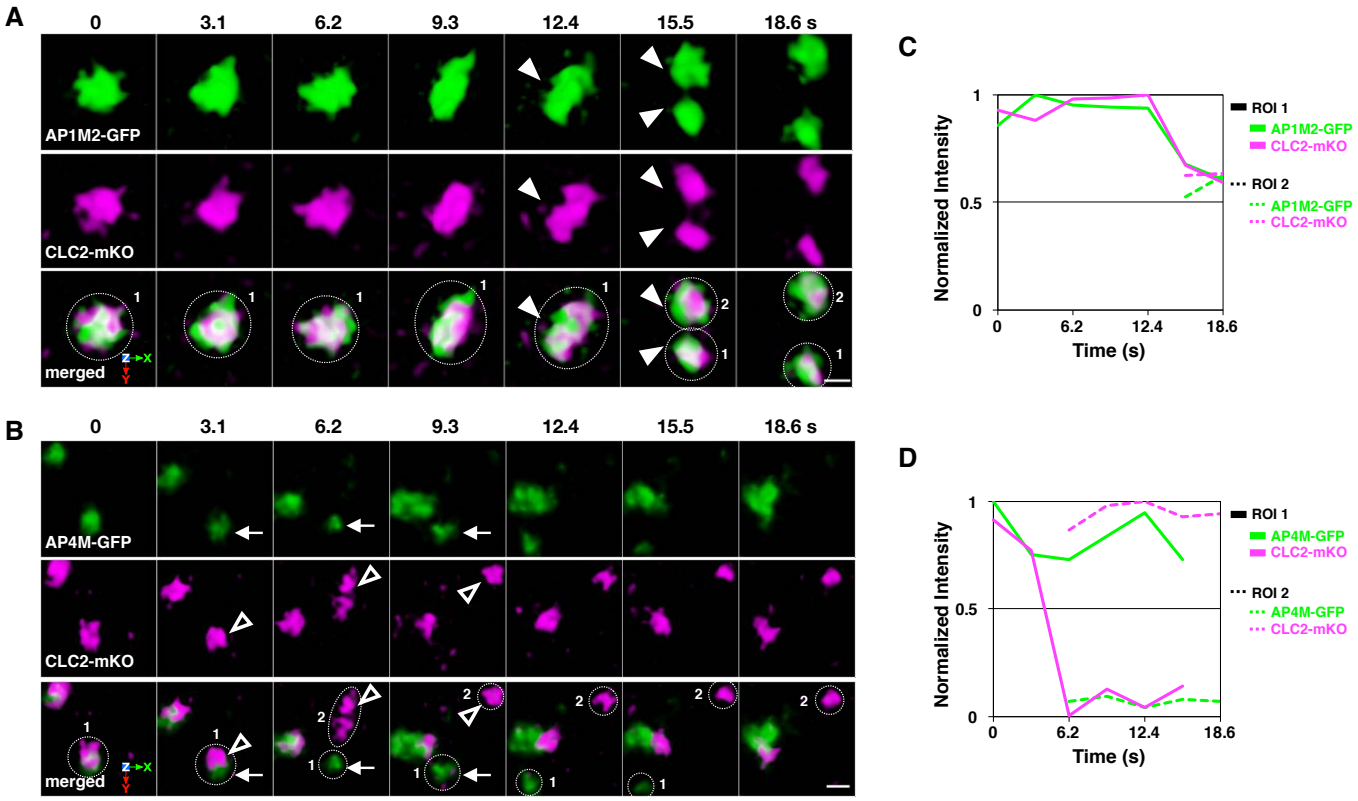

Figure 19. AP-1, but not AP-4, behaves together with and clathrin.
(A and B) 4D images of AP1M2-GFP and CLC2-mKO **(A)** or AP4M-GFP and CLC2-mKO **(B)** in the epidermal cells of the root elongation zone under SCLIM. Arrowheads indicate coincidental AP1M2-GFP and CLC2-mKO signal fission. Open arrowheads indicate dissociation of CLC2-mKO from AP4M-GFP (arrows). Images are lined up every 3.1 s from left to right. Scale bars = 1 μm.
(C and D) Time course changes in relative fluorescence intensities in ROIs of **A** and **B,** respectively.

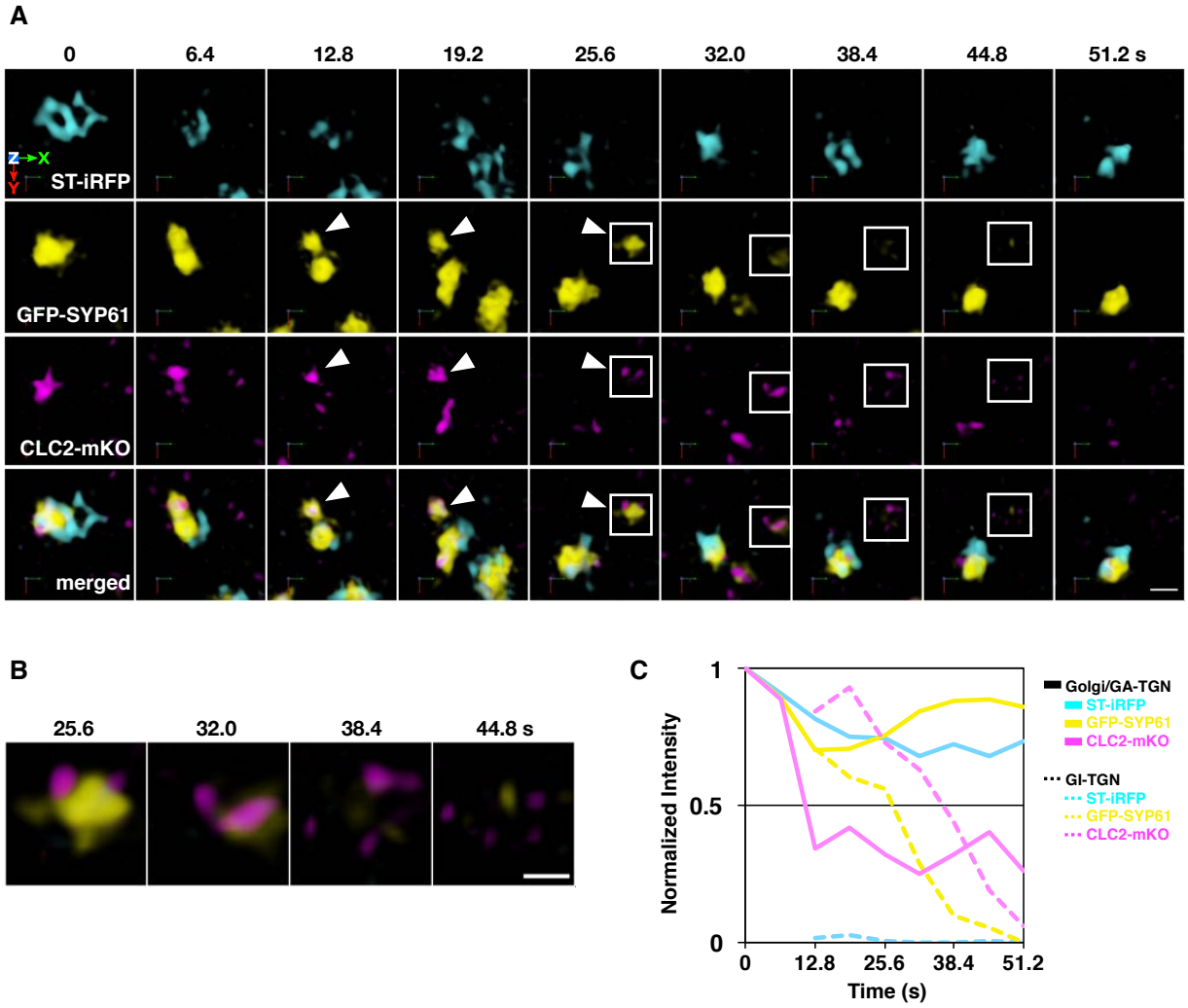

Figure 20. Temporal relation between the Golgi, TGN, and secretory trafficking zone component clathrin. **(A)** 4D images of ST-iRFP, GFP-SYP61, and CLC2-mKO in the epidermal cell of the root elongation zone under SCLIM. White arrowheads indicate dissociation of CLC2 and SYP61 subpopulation from the major population of the TGN (GA-TGN) labelled with GFP-SYP61. **(B)** Magnified images of boxed area in **A**. Images are lined up every 6.4 s from left to right. **(C)** Time course changes in relative fluorescence intensities of ST-iRFP, GFP-SYP61, and CLC2-mKO in the Golgi/GA-TGN or GI-TGN area in **A**. Scale bars = 1 μm **(A)**; 500 nm **(B).**

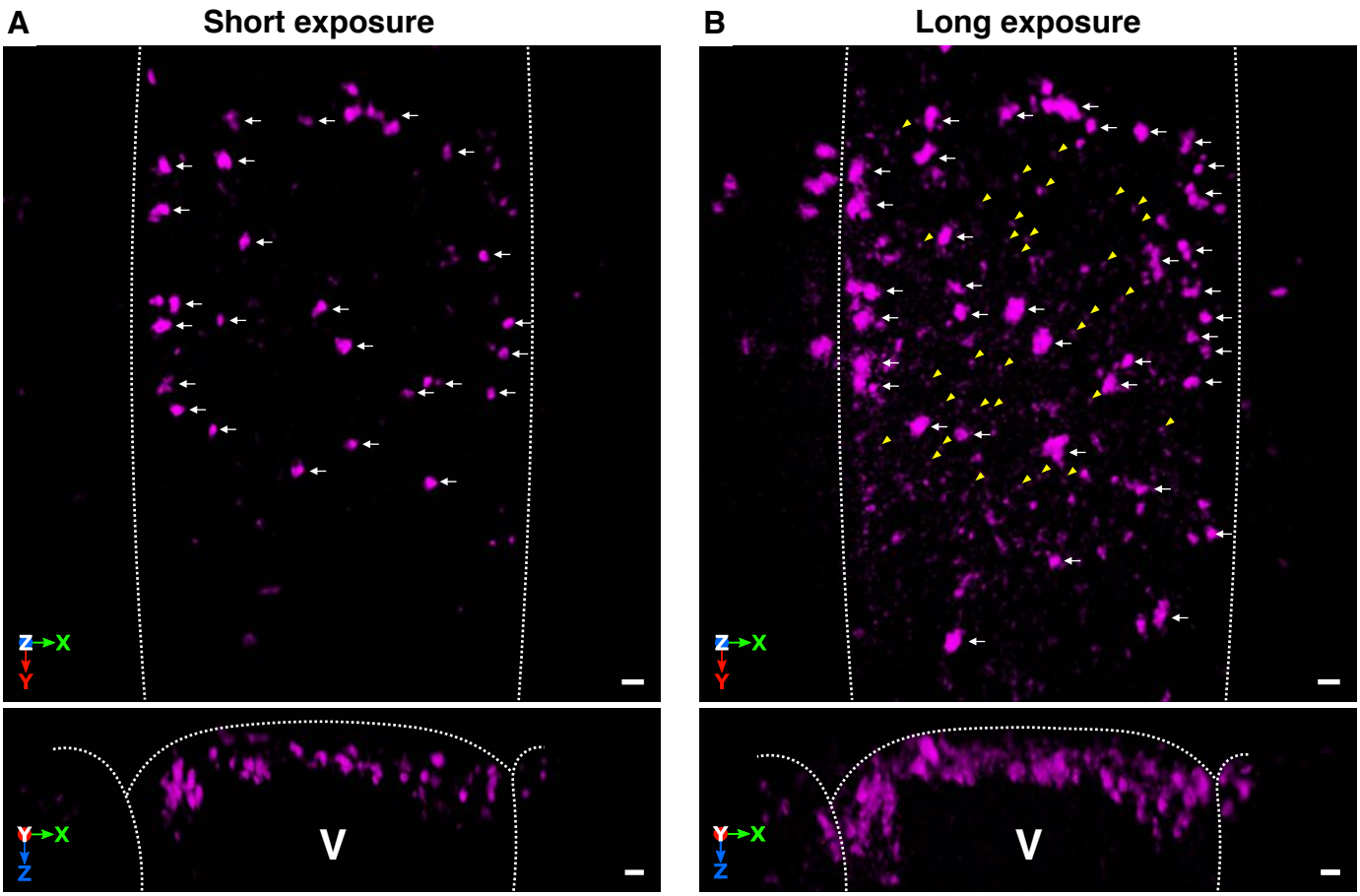

Figure 21. Fluorescent protein-tagged clathrin on the plasma membrane and the endomembrane.
(A and B) Short exposure **(A)** and long exposure **(B)** 3D images of CLC2-mKO in the epidermal cell of the root elongation zone under SCLIM. Arrowheads indicate representative CLC2-mKO signals on the plasma membrane. Arrows indicate TGN-localized CLC2-mKO. Dashed lines show cell edges. V, vacuole area. Scale bars = 1μm.

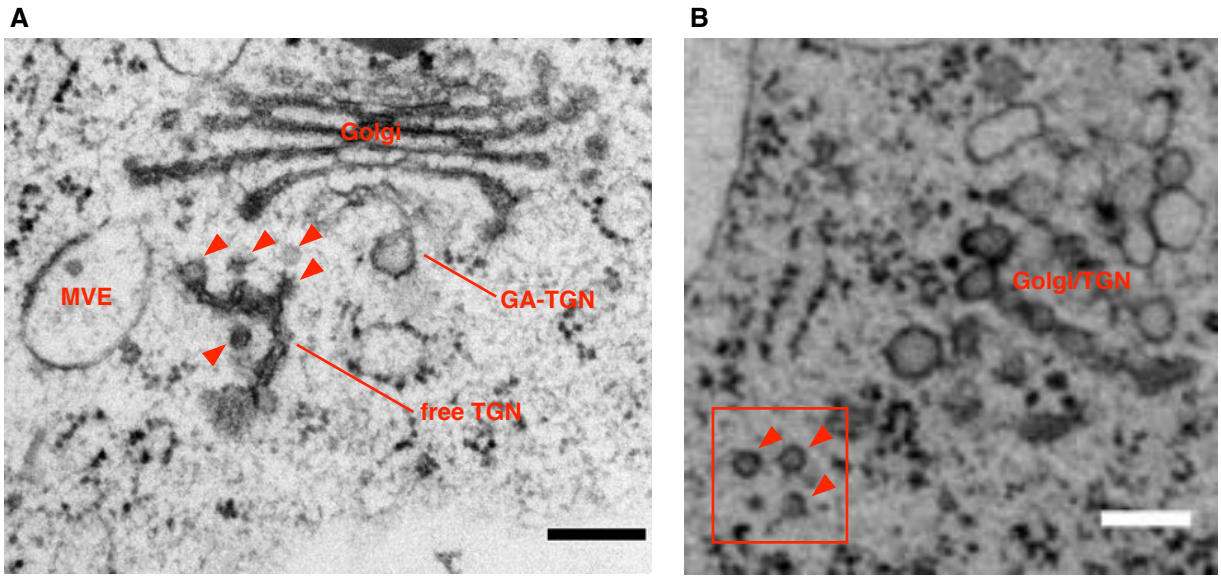

Figure 22. Ultrastructure of the Golgi, TGN, and secretory trafficking zone component clathrin.
(A and B) Transmission electron microscopic images of Arabidopsis root epidermal cells. Arrowheads indicate clathrin-coated vesicles/buds. Boxed area shows the CCV cluster. Scale bars = 200 nm.

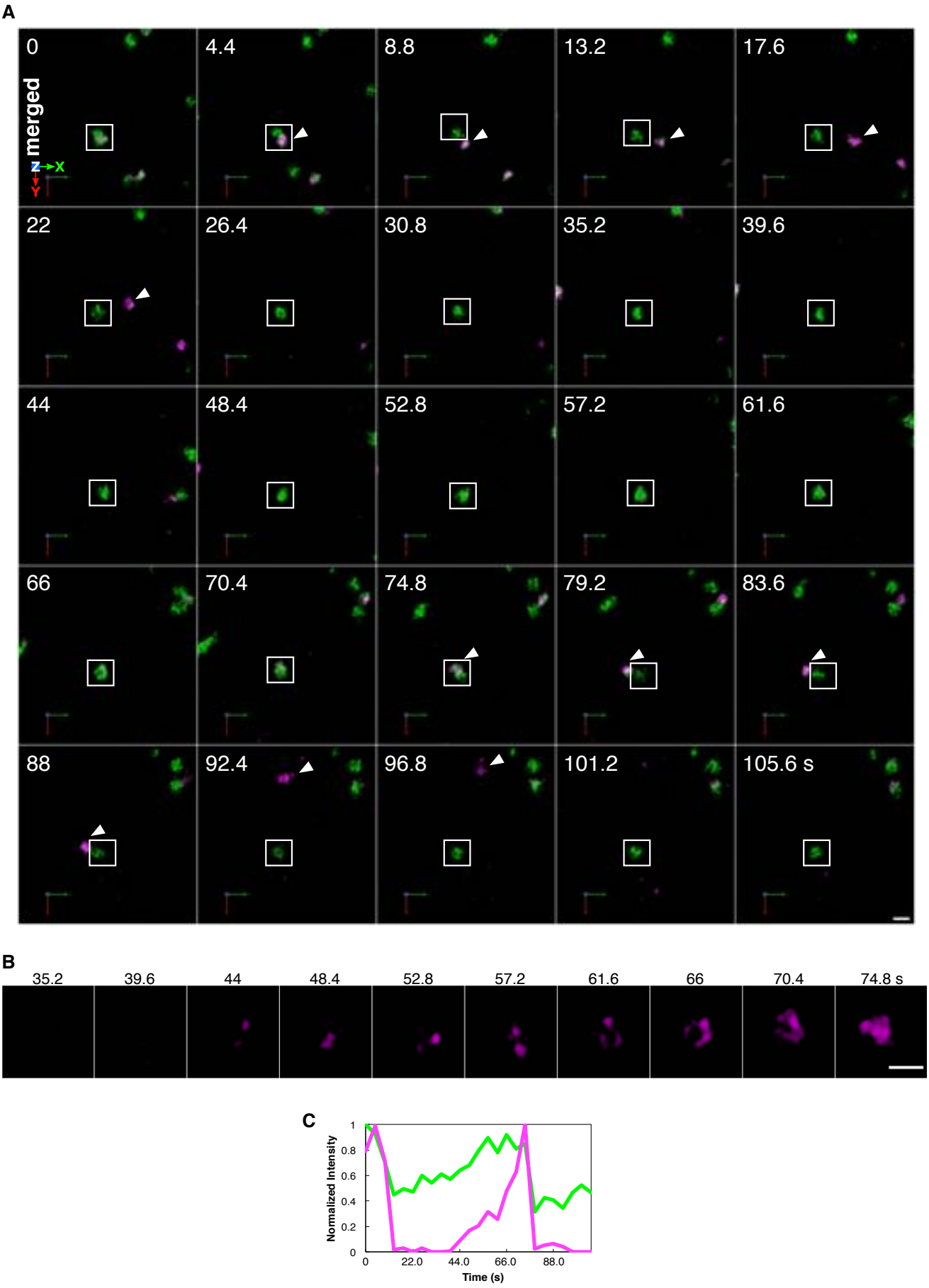

Figure 23. Accumulation and budding of clathrin from the GA-TGN.
(A) 4D images of GFP-SYP61 and CLC2-mKO in the epidermal cell of the root elongation zone under SCLIM. Arrowheads indicate dissociation of the GI-TGN labeled with GFP-SYP61 and CLC2-mKO from the GA-TGN.
(B) Magnified images of CLC2-mKO accumulation on the TGN shown in **A** (35.2 s – 74.8 s). Images are lined up every 4.4 s from left to right. Scale bars = 1 μm.
(C) Temporal fluorescence profiles of boxed area in **A**.

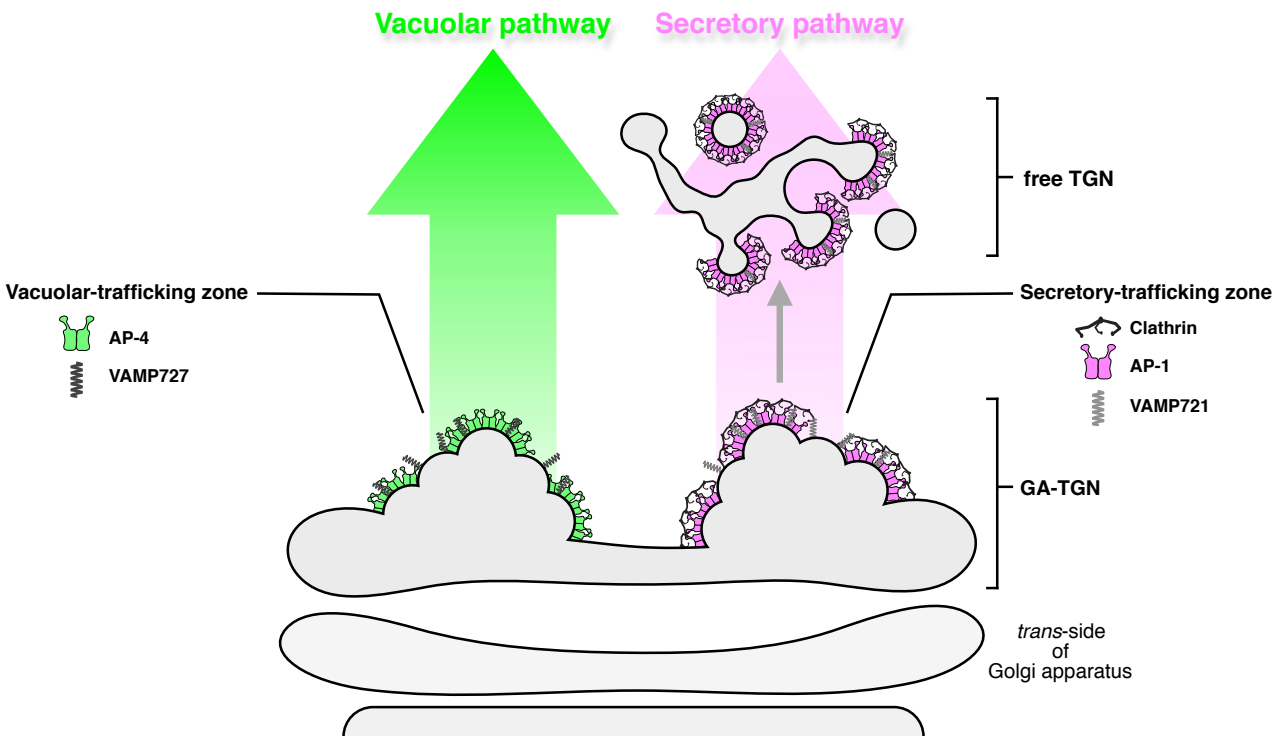

Figure 24. A schematic model of two distinct trafficking zones of the TGN.
The Golgi-associated TGN (GA-TGN) has at least two zones, the secretory-trafficking zone and the vacuolar-trafficking zone, responsible for distinct cargo sorting in Arabidopsis root epidermal cells. The secretory-trafficking zone consists of R-SNARE VAMP721 (pale grey), adaptor protein AP-1 (magenta), and coat protein clathrin (black). The vacuolar-trafficking zone consists of R-SNARE VAMP727 (dark grey) and adaptor protein AP-4 (green). From the secretory-trafficking zone, some of the TGN detaches as the free TGN in a form of a vesicle/bud cluster including clathrin-coated vesicles/buds.

References

Bashline, L., Li, S., Anderson, C. T., Lei, L., & Gu, Y. (2013). The Endocytosis of Cellulose Synthase in Arabidopsis Is Dependent on μ2, a Clathrin-Mediated Endocytosis Adaptin. *Plant Physiology*, *163*(1), 150–160. https://doi.org/10.1104/pp.113.221234

Bassham, D. C., Sanderfoot, A. A., Kovaleva, V., Zheng, H., & Raikhel, N. V. (2000). AtVPS45 complex formation at the trans-Golgi network. *Molecular Biology of the Cell*, *11*(7), 2251–2265. https://doi.org/10.1091/mbc.11.7.2251

Boehm, M., & Bonifacino, J. S. (2001). Adaptins: the final recount. *Molecular Biology of the Cell*, *12*(10), 2907–2920. https://doi.org/10.1091/mbc.12.10.2907

Boevink, P., Oparka, K., Cruz, S. S., Martin, B., Betteridge, A., & Hawes, C. (1998). Stacks on tracks: The plant Golgi apparatus traffics on an actin/ER network. *Plant Journal*, *15*(3), 441–447. https://doi.org/10.1046/j.1365-313X.1998.00208.x

Boncompain, G., Divoux, S., Gareil, N., De Forges, H., Lescure, A., Latreche, L., Mercanti, V., Jollivet, F., Raposo, G., & Perez, F. (2012). Synchronization of secretory protein traffic in populations of cells. *Nature Methods*, *9*(5), 493–498. https://doi.org/10.1038/nmeth.1928

Boutté, Y., & Grebe, M. (2014). Immunocytochemical Fluorescent In Situ Visualization of Proteins In Arabidopsis. In J. J. Sanchez-Serrano & J. Salinas (Eds.), *Arabidopsis Protocols. Methods in Molecular Biology, 1062*, 453–472. Humana Press. https://doi.org/10.1007/978-1-62703-580-4_24

Boutté, Y., Jonsson, K., Mcfarlane, H. E., Johnson, E., Gendre, D., & Swarup, R. (2013). ECHIDNA-mediated post-Golgi trafficking of auxin carriers for differential cell elongation. *Proceedings of the National Academy of Sciences*, *110*(40), 16259–16264. https://doi.org/10.1073/pnas.1309057110

Chen, X., Irani, N. G., & Friml, J. (2011). Clathrin-mediated endocytosis: the gateway into plant cells. *Current Opinion in Plant Biology*, *14*(6), 674–682. https://doi.org/10.1016/j.pbi.2011.08.006

Costes, S. V, Daelemans, D., Cho, E. H., Dobbin, Z., Pavlakis, G., & Lockett, S. (2004). Automatic and Quantitative Measurement of Protein-Protein Colocalization in Live Cells. *Biophysical Journal*, *86*, 3993–4003. https://doi.org/10.1529/biophysj.103.038422

Cui, Y., Shen, J., Gao, C., Zhuang, X., Wang, J., & Jiang, L. (2016). Biogenesis of Plant Prevacuolar Multivesicular Bodies. *Molecular Plant*, *9*(6), 774–786. https://doi.org/10.1016/j.molp.2016.01.011

Dacks, J. B., & Robinson, M. S. (2017). Outerwear through the ages: evolutionary cell biology of vesicle coats. *Current Opinion in Cell Biology*, *47*, 108–116. https://doi.org/10.1016/j.ceb.2017.04.001

Day, K. J., Staehelin, L. A., & Glick, B. S. (2013). A three-stage model of Golgi structure and function.

Histochemistry and Cell Biology, *140*(3), 239–249. https://doi.org/10.1007/s00418-013-1128-3

Dell'Angelica, E. C. (2001). Clathrin-binding proteins: Got a motif? Join the network! *Trends in Cell Biology*, *11*(8), 315–318. https://doi.org/10.1016/S0962-8924(01)02043-8

Derby, M. C., & Gleeson, P. A. (2007). New Insights into Membrane Trafficking and Protein Sorting. *International Review of Cytology*, *261*(07), 47–116. https://doi.org/10.1016/S0074-7696(07)61002-X

Dettmer, J., Hong-Hermesdorf, A., Stierhof, Y.-D., & Schumacher, K. (2006). Vacuolar H+-ATPase Activity Is Required for Endocytic and Secretory Traf cking in Arabidopsis. *The Plant Cell*, *18*, 715–730. https://doi.org/10.1105/tpc.105.037978.null

Di Rubbo, S., Irani, N. G., Kim, S. Y., Xu, Z.-Y., Gadeyne, A., Dejonghe, W., Vanhoutte, I., Persiau, G., Eeckhout, D., Simon, S., Song, K., Kleine-Vehn, J., Friml, J., De Jaeger, G., Van Damme, D., Hwang, I., & Russinova, E. (2013). The Clathrin Adaptor Complex AP-2 Mediates Endocytosis of BRASSINOSTEROID INSENSITIVE1 in Arabidopsis. *The Plant Cell*, *25*(8), 2986–2997. https://doi.org/10.1105/tpc.113.114058

Doray, B., & Kornfeld, S. (2001). γ Subunit of the AP-1 adaptor complex binds clathrin: Implications for cooperative binding in coated vesicle assembly. *Molecular Biology of the Cell*, *12*(7), 1925–1935. https://doi.org/10.1091/mbc.12.7.1925

Ebine, K., Fujimoto, M., Okatani, Y., Nishiyama, T., Goh, T., Ito, E., Dainobu, T., Nishitani, A., Uemura, T., Sato, M. H., Thordal-Christensen, H., Tsutsumi, N., Nakano, A., & Ueda, T. (2011). A membrane trafficking pathway regulated by the plant-specific RAB GTPase ARA6. *Nature Cell Biology*, *13*(7), 853–859. https://doi.org/10.1038/ncb2270

Ebine, K., Okatani, Y., Uemura, T., Goh, T., Shoda, K., Niihama, M., Morita, M. T., Spitzer, C., Otegui, M. S., Nakano, A., & Ueda, T. (2008). A SNARE complex unique to seed plants is required for protein storage vacuole biogenesis and seed development of Arabidopsis thaliana. *The Plant Cell*, *20*(11), 3006–3021. https://doi.org/10.1105/tpc.107.057711

El Kasmi, F., Krause, C., Hiller, U., Stierhof, Y. D., Mayer, U., Conner, L., Kong, L., Reichardt, I., Sanderfoot, A. A., & Jürgens, G. (2013). SNARE complexes of different composition jointly mediate membrane fusion in Arabidopsis cytokinesis. *Molecular Biology of the Cell*, *24*(10), 1593–1601. https://doi.org/10.1091/mbc.E13-02-0074

Filonov, G. S., Piatkevich, K. D., Ting, L., Zhang, J., Kim, K., & Verkhusha, V. V. (2011). Bright and stable near-infrared fluorescent protein for in vivo imaging. *Nature Biotechnology*, *29*(8), 757–761. https://doi.org/10.1038/nbt.1918

Fuji, K., Shirakawa, M., Shimono, Y., Kunieda, T., Fukao, Y., Koumoto, Y., Takahashi, H.,

Hara-Nishimura, I., & Shimada, T. (2016). The Adaptor Complex AP-4 Regulates Vacuolar Protein Sorting at the trans-Golgi Network by Interacting with VACUOLAR SORTING RECEPTOR1. *Plant Physiology*, *170*(1), 211–219. https://doi.org/10.1104/pp.15.00869

Fujii, S., Kurokawa, K., Inaba, R., Hiramatsu, N., Tago, T., Nakamura, Y., Nakano, A., Satoh, T., & Satoh, A. K. (2020). Recycling endosomes attach to the trans-side of Golgi stacks in Drosophila and mammalian cells. *Journal of Cell Science*, *133*(4), jcs236935. https://doi.org/10.1242/jcs.236935

Fujimoto, M., & Ueda, T. (2012). Conserved and plant-unique mechanisms regulating plant post-Golgi traffic. *Frontiers in Plant Science*, *3*, 1–10. https://doi.org/10.3389/fpls.2012.00197

Gendre, D., McFarlane, H. E., Johnson, E., Mouille, G., Sjodin, A., Oh, J., Levesque-Tremblay, G., Watanabe, Y., Samuels, L., & Bhalerao, R. P. (2013). Trans-Golgi Network Localized ECHIDNA/Ypt Interacting Protein Complex Is Required for the Secretion of Cell Wall Polysaccharides in Arabidopsis. *The Plant Cell*, *25*(7), 2633–2646. https://doi.org/10.1105/tpc.113.112482

Gendre, D., Oh, J., Boutte, Y., Best, J. G., Samuels, L., Nilsson, R., Uemura, T., Marchant, A., Bennett, M. J., Grebe, M., & Bhalerao, R. P. (2011). Conserved Arabidopsis ECHIDNA protein mediates trans-Golgi-network trafficking and cell elongation. *Proceedings of the National Academy of Sciences*, *108*(19), 8048–8053. https://doi.org/10.1073/pnas.1018371108

Gershlick, D. C., De Marcos Lousa, C., Foresti, O., Lee, A. J., Pereira, E. A., daSilva, L. L. P., Bottanelli, F., & Denecke, J. (2014). Golgi-dependent transport of vacuolar sorting receptors is regulated by COPII, AP1, and AP4 protein complexes in tobacco. *Plant Cell*, *26*(3), 1308–1329. https://doi.org/10.1105/tpc.113.122226

Glick, B. S., & Nakano, A. (2009). Membrane Traffic Within the Golgi Apparatus. *Annual Review of Cell and Developmental Biology*, *25*(1), 113–132. https://doi.org/10.1146/annurev.cellbio.24.110707.175421

Goh, T., Uchida, W., Arakawa, S., Ito, E., Dainobu, T., Ebine, K., Takeuchi, M., Sato, K., Ueda, T., & Nakano, A. (2007). VPS9a, the common activator for two distinct types of Rab5 GTPases, is essential for the development of Arabidopsis thaliana. *Plant Cell*, *19*(11), 3504–3515. https://doi.org/10.1105/tpc.107.053876

Goldfischer, S. (1982). The internal reticular apparatus of Camillo Golgi: a complex, heterogeneous organelle, enriched in acid, neutral, and alkaline phosphatases, and involved in glycosylation, secretion, membrane flow, lysosome formation, and intracellular digestion. *Journal of Histochemistry & Cytochemistry*, *30*(7), 717–733. https://doi.org/https://doi.org/10.1177/30.7.6286754

Griffiths, G., & Simons, K. (1986). The trans Golgi network: Sorting at the Exit Site of the Golgi Complex. *Science*, *234*(4775), 438–443. https://doi.org/10.1126/science.2945253

Hand, A. R. (1980). Cytochemical differentiation of the Golgi apparatus from GERL. *The Journal of Histochemistry and Cytochemistry : Official Journal of the Histochemistry Society*, *28*(1), 82–86. https://doi.org/10.1177/28.1.7351475

Hirst, J., Barlow, L. D., Francisco, G. C., Sahlender, D. A., Seaman, M. N. J., Dacks, J. B., & Robinson, M. S. (2011). The fifth adaptor protein complex. *PLoS Biol*, *9*(10), e1001170. https://doi.org/10.1371/journal.pbio.1001170

Huang, Y., Ma, T., Lau, P. K., Wang, J., Zhao, T., Du, S., Loy, M. M. T., & Guo, Y. (2019). Visualization of Protein Sorting at the Trans-Golgi Network and Endosomes Through Super-Resolution Imaging. *Frontiers in Cell and Developmental Biology*, *7*, 181. https://doi.org/10.3389/fcell.2019.00181

Ito, E., Fujimoto, M., Ebine, K., Uemura, T., Ueda, T., & Nakano, A. (2012). Dynamic behavior of clathrin in Arabidopsis thaliana unveiled by live imaging. *Plant Journal*, *69*(2), 204–216. https://doi.org/10.1111/j.1365-313X.2011.04782.x

Ito, Y., & Boutté, Y. (2020). Differentiation of Trafficking Pathways at Golgi Entry Core Compartments and Post-Golgi Subdomains. *Frontiers in Plant Science*, *11*(December). https://doi.org/10.3389/fpls.2020.609516

Ito, Y., Uemura, T., & Nakano, A. (2018). The Golgi entry core compartment functions as a COPII-independent scaffold for ER-to-Golgi transport in plant cells. *Journal of Cell Science*, *131*(2). https://doi.org/10.1242/jcs.203893

Jonsson, K., Singh, R. K., Gendre, D., & Bhalerao, R. P. (2017). *Ethylene Regulates Differential Growth via BIG ARF-GEF-Dependent Post-Golgi Secretory Traf fi cking in Arabidopsis*. *29*, 1039–1052. https://doi.org/10.1105/tpc.16.00743

Kang, B.-H., Nielsen, E., Preuss, M. L., Mastronarde, D., & Staehelin, L. A. (2011). Electron Tomography of RabA4b- and PI-4Kβ1-Labeled Trans Golgi Network Compartments in Arabidopsis. *Traffic*, *12*(3), 313–329. https://doi.org/10.1111/j.1600-0854.2010.01146.x

Keen, J. H. (1987). Clathrin assembly proteins: Affinity purification and a model for coat assembly. *Journal of Cell Biology*, *105*(5), 1989–1998. https://doi.org/10.1083/jcb.105.5.1989

Kim, S. Y., Xu, Z.-Y., Song, K., Kim, D. H., Kang, H., Reichardt, I., Sohn, E. J., Friml, J., Juergens, G., & Hwang, I. (2013). Adaptor Protein Complex 2-Mediated Endocytosis Is Crucial for Male Reproductive Organ Development in Arabidopsis. *The Plant Cell*, *25*(8), 2970–2985. https://doi.org/10.1105/tpc.113.114264

Klumperman, J. (2011). Architecture of the mammalian Golgi. *Cold Spring Harbor Perspectives in*

Biology, *3*(7), 1–19. https://doi.org/10.1101/cshperspect.a005181

Koike, S., & Jahn, R. (2019). SNAREs define targeting specificity of trafficking vesicles by combinatorial interaction with tethering factors. *Nature Communications*, *10*(1). https://doi.org/10.1038/s41467-019-09617-9

Kurokawa, K., Ishii, M., Suda, Y., Ichihara, A., & Nakano, A. (2013). Live cell visualization of golgi membrane dynamics by super-resolution confocal live imaging microscopy. In *Methods in Cell Biology* (1st ed., Vol. 118). Elsevier Inc. https://doi.org/10.1016/B978-0-12-417164-0.00014-8

Kurokawa, K., Osakada, H., Kojidani, T., Waga, M., Suda, Y., Asakawa, H., Haraguchi, T., & Nakano, A. (2019). Visualization of secretory cargo transport within the Golgi apparatus. *Journal of Cell Biology*, *218*(5), 1602–1618. https://doi.org/10.1083/jcb.201807194

Kurokawa, K. & Nakano, A. (2020). Live-cell Imaging by Super-resolution Confocal Live Imaging Microscopy (SCLIM): Simultaneous Three-color and Four-dimensional Live Cell Imaging with High Space and Time Resolution. *Bio-protocol*, *10*(17), e3732. DOI: 10.21769/BioProtoc.3732

Kwon, C., Neu, C., Pajonk, S., Yun, H. S., Lipka, U., Humphry, M., Bau, S., Straus, M., Kwaaitaal, M., Rampelt, H., Kasmi, F. El, Jürgens, G., Parker, J., Panstruga, R., Lipka, V., & Schulze-Lefert, P. (2008). Co-option of a default secretory pathway for plant immune responses. *Nature*, *451*(7180), 835–840. https://doi.org/10.1038/nature06545

Lemmon, S. K., & Traub, L. M. (2012). Getting in Touch with the Clathrin Terminal Domain. *Traffic*, *13*(4), 511–519. https://doi.org/10.1111/j.1600-0854.2011.01321.x

Lipka, V., Kwon, C., & Panstruga, R. (2007). SNARE-Ware: The Role of SNARE-Domain Proteins in Plant Biology. *Annual Review of Cell and Developmental Biology*, *23*(1), 147–174. https://doi.org/10.1146/annurev.cellbio.23.090506.123529

McMahon, H. T., & Boucrot, E. (2011). Molecular mechanism and physiological functions of clathrin-mediated endocytosis. *Nature Reviews Molecular Cell Biology*, *12*(8), 517–533. https://doi.org/10.1038/nrm3151

Mellman, I., & Warren, G. (2000). *The Road Taken : Past and Future Foundations of Membrane Traffic*. *100*, 99–112.

Miller, S. E., Collins, B. M., McCoy, A. J., Robinson, M. S., & Owen, D. J. (2007). A SNARE-adaptor interaction is a new mode of cargo recognition in clathrin-coated vesicles. *Nature*, *450*(7169), 570–574. https://doi.org/10.1038/nature06353

Miller, S. E., Sahlender, D. A., Graham, S. C., Höning, S., Robinson, M. S., Peden, A. A., & Owen, D. J. (2011). The molecular basis for the endocytosis of small R-SNAREs by the clathrin adaptor CALM.

Cell, *147*(5), 1118–1131. https://doi.org/10.1016/j.cell.2011.10.038

Minamino, N., & Ueda, T. (2019). RAB GTPases and their effectors in plant endosomal transport. *Current Opinion in Plant Biology*, *52*, 61–68. https://doi.org/10.1016/j.pbi.2019.07.007

Müdsam, C., Wollschläger, P., Sauer, N., & Schneider, S. (2018). Sorting of Arabidopsis NRAMP3 and NRAMP4 depends on adaptor protein complex AP4 and a dileucine-based motif. *Traffic*, *19*(7), 503–521. https://doi.org/10.1111/tra.12567

Nakano, A. (2013). Super-resolution confocal live imaging microscopy (SCLIM) — Cutting-edge technology in cell biology. *2013 35th Annual International Conference of the IEEE Engineering in Medicine and Biology Society (EMBC)*, 133–135. https://doi.org/10.1109/EMBC.2013.6609455

Narasimhan, M., Johnson, A., Prizak, R., Kaufmann, W. A., Tan, S., Casillas-Pérez, B., & Friml, J. (2020). Evolutionarily unique mechanistic framework of clathrin-mediated endocytosis in plants. *ELife*, *9*, 1–30. https://doi.org/10.7554/elife.52067

Nishi, T., & Forgac, M. (2002). THE VACUOLAR (H^+)-ATPASES — NATURE'S MOST VERSATILE PROTON PUMPS. *Nature Reviews Molecular Cell Biology*, *3*(February), 94–103. https://doi.org/10.1038/nrm729

Novikoff, A. B. (1964). GERL, its form and functions in neurons of rat spinal ganglia. *Biol.Bull.*, *127*, 358A. http://ci.nii.ac.jp/naid/10004489818/ja/

Novikoff, A. B. (1976). The endoplasmic reticulum: a cytochemist's view (a review). *Proceedings of the National Academy of Sciences*, *73*(8), 2781–2787. https://doi.org/10.1073/PNAS.73.8.2781

Novikoff, A. B., Mori, M., Quintana, N., & Yam, A. (1977). Studies of the secretory process in the mammalian exocrine pancreas. I. The condensing vacuoles. *Journal of Cell Biology*, *75*(1), 148–165. https://doi.org/10.1083/jcb.75.1.148

Novikoff, P. M., Novikoff, A. B., Quintana, N., & Hauw, J. J. (1971). Golgi apparatus, gerl, and lysosomes of neurons in rat dorsal root ganglia, studied by thick section and thin section cytochemistry. *Journal of Cell Biology*, *50*(3), 859–886. https://doi.org/10.1083/jcb.50.3.859

Ohgane, K. (2019). Quantification of Gel Bands by an Image J Macro, Band/Peak Quantification Tool. *Protocols.Io*, 1–10. https://doi.org/dx.doi.org/10.17504/protocols.io.7vghn3w

Paczkowski, J. E., Richardson, B. C., & Fromme, J. C. (2015). Cargo adaptors: Structures illuminate mechanisms regulating vesicle biogenesis. *Trends in Cell Biology*, *25*(7), 408–416. https://doi.org/10.1016/j.tcb.2015.02.005

Park, M., Song, K., Reichardt, I., Kim, H., Mayer, U., Stierhof, Y.-D., Hwang, I., & Jürgens, G. (2013). Arabidopsis μ-adaptin subunit AP1M of adaptor protein complex 1 mediates late secretory and vacuolar traffic and is required for growth. *Proceedings of the National Academy of Sciences of the*

United States of America, *110*(25), 10318–10323. https://doi.org/10.1073/pnas.1300460110

Pryor, P. R., Jackson, L., Gray, S. R., Edeling, M. A., Thompson, A., Sanderson, C. M., Evans, P. R., Owen, D. J., & Luzio, J. P. (2008). Molecular Basis for the Sorting of the SNARE VAMP7 into Endocytic Clathrin- Coated Vesicles by the ArfGAP Hrb. *Cell*, *134*(5), 817–827. https://doi.org/10.1016/j.cell.2008.07.023

Rambourg, a, Clermont, Y., & Hermo, L. (1979). Three-dimensional architecture of the golgi apparatus in Sertoli cells of the rat. *The American Journal of Anatomy*, *154*, 455–476. https://doi.org/10.1002/aja.1001540402

Ren, X., Farías, G. G., Canagarajah, B. J., Bonifacino, J. S., & Hurley, J. H. (2013). Structural basis for recruitment and activation of the AP-1 clathrin adaptor complex by Arf1. *Cell*, *152*(4), 755–767. https://doi.org/10.1016/j.cell.2012.12.042

Renna, L., Stefano, G., Slabaugh, E., Wormsbaecher, C., Sulpizio, A., Zienkiewicz, K., & Brandizzi, F. (2018). TGNap1 is required for microtubule-dependent homeostasis of a subpopulation of the plant trans-Golgi network. *Nature Communications*, *9*(1), 5313. https://doi.org/10.1038/s41467-018-07662-4

Robinson, D. G., & Pimpl, P. (2014). Clathrin and post-Golgi trafficking: A very complicated issue. *Trends in Plant Science*, *19*(3), 134–139. https://doi.org/10.1016/j.tplants.2013.10.008

Robinson, M. S., & Bonifacino, J. S. (2001). Adaptor-related proteins. *Current Opinion in Cell Biology*, *13*(4), 444–453. https://doi.org/10.1016/S0955-0674(00)00235-0

Roth, J. (1985). Demonstration of an extensive trans-tubular network continuous with the Golgi apparatus stack that may function in glycosylation. *Cell*, *43*(1), 287–295. https://doi.org/10.1016/0092-8674(85)90034-0

Saito, C., & Ueda, T. (2009). Functions of RAB and SNARE Proteins in Plant Life. In *International Review of Cell and Molecular Biology* (1st ed., Vol. 274). Elsevier Inc. https://doi.org/10.1016/S1937-6448(08)02004-2

Sanderfoot, A. A., Kovaleva, V., Bassham, D. C., & Raikhel, N. V. (2001). Interactions between syntaxins identify at least five SNARE complexes within the Golgi/prevacuolar system of the Arabidopsis cell. *Molecular Biology of the Cell*, *12*(12), 3733–3743. https://doi.org/10.1091/mbc.12.12.3733

Shimada, T., Kunieda, T., Sumi, S., Koumoto, Y., Tamura, K., Hatano, K., Ueda, H., & Hara-Nishimura, I. (2018). The AP-1 Complex is Required for Proper Mucilage Formation in Arabidopsis Seeds. *Plant & Cell Physiology*, *59*(11), 2331–2338. https://doi.org/10.1093/pcp/pcy158

Singh, M. K., & Jürgens, G. (2018). Specificity of plant membrane trafficking – ARFs, regulators and coat proteins. *Seminars in Cell and Developmental Biology*, *80*, 85–93.

https://doi.org/10.1016/j.semcdb.2017.10.005

Staehelin, L. A., & Kang, B.-H. (2008). Nanoscale Architecture of Endoplasmic Reticulum Export Sites and of Golgi Membranes as Determined by Electron Tomography. *Plant Physiology*, *147*(4), 1454–1468. https://doi.org/10.1104/pp.108.120618

Staehelin, L. A., & Moore, I. (1995). The Plant Golgi Apparatus: Structure, Functional Organization and Trafficking Mechanisms. *Annual Review of Plant Physiology and Plant Molecular Biology*, *46*(1), 261–288. https://doi.org/10.1146/annurev.pp.46.060195.001401

Teh, O. K., Shimono, Y., Shirakawa, M., Fukao, Y., Tamura, K., Shimada, T., & Hara-Nishimura, I. (2013). The AP-1 μ Adaptin is Required for KNOLLE Localization at the Cell Plate to Mediate Cytokinesis in Arabidopsis. *Plant and Cell Physiology*, *54*(6), 838–847. https://doi.org/10.1093/pcp/pct048

Teo, M., Tan, L., Lim, L., & Manser, E. (2001). The Tyrosine Kinase ACK1 Associates with Clathrin-coated Vesicles through a Binding Motif Shared by Arrestin and Other Adaptors. *Journal of Biological Chemistry*, *276*(21), 18392–18398. https://doi.org/10.1074/jbc.M008795200

Tojima, T., Suda, Y., Ishii, M., Kurokawa, K., & Nakano, A. (2019). Spatiotemporal dissection of the *trans*-Golgi network in budding yeast. *Journal of Cell Science*, *132*(15), jcs231159. https://doi.org/10.1242/jcs.231159

Toyooka, K., Goto, Y., Asatsuma, S., Koizumi, M., Mitsui, T., & Matsuoka, K. (2009). A Mobile Secretory Vesicle Cluster Involved in Mass Transport from the Golgi to the Plant Cell Exterior. *The Plant Cell*, *21*(4), 1212–1229. https://doi.org/10.1105/tpc.108.058933

Ueda, T., Yamaguchi, M., Uchimiya, H., & Nakano, A. (2001). Ara6, a plant-unique novel type Rab GTPase, functions in the endocytic pathway of Arabidopsis thaliana. *EMBO Journal*, *20*(17), 4730–4741. https://doi.org/10.1093/emboj/20.17.4730

Uemura, T. (2016). Physiological roles of plant post-golgi transport pathways in membrane trafficking. *Plant and Cell Physiology*, *57*(10), 2013–2019. https://doi.org/10.1093/pcp/pcw149

Uemura, T., Kim, H., Saito, C., Ebine, K., Ueda, T., Schulze-Lefert, P., & Nakano, A. (2012). Qa-SNAREs localized to the trans-Golgi network regulate multiple transport pathways and extracellular disease resistance in plants. *Proceedings of the National Academy of Sciences of the United States of America*, *109*(5), 1784–1789. https://doi.org/10.1073/pnas.1115146109

Uemura, T., Nakano, R. T., Takagi, J., Wang, Y., Kramer, K., Finkemeier, I., Nakagami, H., Tsuda, K., Ueda, T., Schulze-Lefert, P., & Nakano, A. (2019). A Golgi-released subpopulation of the trans-Golgi network mediates protein secretion in Arabidopsis. *Plant Physiology*, *179*(February), pp.01228.2018. https://doi.org/10.1104/pp.18.01228

Uemura, T., Suda, Y., Ueda, T., & Nakano, A. (2014). Dynamic behavior of the trans-golgi network in root

tissues of arabidopsis revealed by super-resolution live imaging. *Plant and Cell Physiology*, *55*(4), 694–703. https://doi.org/10.1093/pcp/pcu010

Uemura, T., Ueda, T., Ohniwa, R. L., Nakano, A., Takeyasu, K., & Sato, M. H. (2004). Systematic analysis of SNARE molecules in Arabidopsis: dissection of the post-Golgi network in plant cells. *Cell Structure and Function*, *29*(2), 49–65. https://doi.org/10.1247/csf.29.49

Viotti, C., Bubeck, J., Stierhof, Y.-D., Krebs, M., Langhans, M., van den Berg, W., van Dongen, W., Richter, S., Geldner, N., Takano, J., Jürgens, G., de Vries, S. C., Robinson, D. G., & Schumacher, K. (2010). Endocytic and secretory traffic in Arabidopsis merge in the trans-Golgi network/early endosome, an independent and highly dynamic organelle. *Plant Cell*, *22*(4), 1344–1357. https://doi.org/10.1105/tpc.109.072637

Wang, J.-G., Feng, C., Liu, H.-H., Feng, Q.-N., Li, S., & Zhang, Y. (2017). AP1G mediates vacuolar acidification during synergid-controlled pollen tube reception. *Proceedings of the National Academy of Sciences*, *114*(24), E4877–E4883. https://doi.org/10.1073/pnas.1617967114

Wang, J.-G., Feng, C., Liu, H. H., Ge, F. R., Li, S., Li, H. J., & Zhang, Y. (2016). HAPLESS13-Mediated Trafficking of STRUBBELIG Is Critical for Ovule Development in Arabidopsis. *PLoS Genetics*, *12*(8), 1–21. https://doi.org/10.1371/journal.pgen.1006269

Wang, J.-G., Li, S., Zhao, X.-Y., Zhou, L.-Z., Huang, G.-Q., Feng, C., & Zhang, Y. (2013). HAPLESS13, the Arabidopsis μ1 Adaptin, Is Essential for Protein Sorting at the trans-Golgi Network/Early Endosome. *Plant Physiology*, *162*(4), 1897–1910. https://doi.org/10.1104/pp.113.221051

Wang, X., Cai, Y., Wang, H., Zeng, Y., Zhuang, X., Li, B., Jiang, L., & Jiang, L. (2014). Trans-Golgi Network-Located AP1 Gamma Adaptins Mediate Dileucine Motif-Directed Vacuolar Targeting in Arabidopsis. *The Plant Cell*, *26*(10), 4102–4118. https://doi.org/10.1105/tpc.114.129759

Wattelet-Boyer, V., Brocard, L., Jonsson, K., Esnay, N., Joubès, J., Domergue, F., Mongrand, S., Raikhel, N., Bhalerao, R. P., Moreau, P., & Boutté, Y. (2016). Enrichment of hydroxylated C24- and C26-acyl-chain sphingolipids mediates PIN2 apical sorting at trans-Golgi network subdomains. *Nature Communications*, *7*, 12788. https://doi.org/10.1038/ncomms12788

Yamaoka, S., Shimono, Y., Shirakawa, M., Fukao, Y., Kawase, T., Hatsugai, N., Tamura, K., Shimada, T., & Hara-nishimura, I. (2013). Identification and Dynamics of Arabidopsis Adaptor Protein-2 Complex and Its Involvement in Floral Organ Development. *The Plant Cell*, *25*(August), 2958–2969. https://doi.org/10.1105/tpc.113.114082

Zhang, L., Zhang, H., Liu, P., Hao, H., Jin, J. B., & Lin, J. (2011). Arabidopsis R-SNARE proteins VAMP721 and VAMP722 are required for cell plate formation. *PLoS ONE*, *6*(10). https://doi.org/10.1371/journal.pone.0026129